THE ASTROPHYSICAL JOURNAL, 907:109 (18pp), 2021 February 1 https://doi.org/10.3847/1538-4357/abd5c2

Dynamics and Emission of Wind-powered Afterglows of Gamma-Ray Bursts: Flares, Plateaus, and Steep Decays

Maxim V. Barkov[1], Yonggang Luo[2], and Maxim Lyutikov[2]
[1] Institute of Astronomy, Russian Academy of Sciences, Moscow, 119017, Russia; barkov@inasan.ru
[2] Department of Physics and Astronomy, Purdue University, 525 Northwestern Avenue, West Lafayette, IN 47907-2036, USA

Received 2020 May 8; revised 2020 December 17; accepted 2020 December 21; published 2021 February 5

Abstract

We have developed a model of early X-ray afterglows of gamma-ray bursts originating from the reverse shock (RS) propagating through ultrarelativistic, highly magnetized pulsar-like winds produced by long-lasting central engines. We first performed fluid and magnetohydrodynamic numerical simulations of relativistic double explosions. We demonstrate that even for constant properties of the wind a variety of temporal behaviors can be produced, depending on the energy of the initial explosion and the wind power, the delay time for the switch-on of the wind, and the magnetization of the wind. X-ray emission of the highly magnetized RS occurs in the fast-cooling regime—this ensures high radiative efficiency and allows fast intensity variations. We demonstrate that (i) RS emission naturally produces light curves, showing power-law temporal evolution with various temporal indices; (ii) mild wind power, of the order of $\sim 10^{46}$ erg s^{-1} (equivalent isotropic), can reproduce the afterglows' plateau phase; (iii) termination of the wind can produce sudden steep decays; and (iv) short-duration afterglow flares are due to mild variations in the wind luminosity, with small total injected energy.

Unified Astronomy Thesaurus concepts: Gamma-ray bursts (629); Magnetohydrodynamics (1964); Non-thermal radiation sources (1119); X-ray transient sources (1852)

1. Introduction

Gamma-ray bursts (GRBs) are produced in relativistic explosions (Paczynski 1986; Piran 2004) that generate two shocks: forward shock (FS) and reversed shock (RS). The standard fireball model (Rees & Meszaros 1992; Sari & Piran 1995; Piran 1999; Mészáros 2006) postulates that the prompt emission is produced by internal dissipative processes within the flow: collisions of matter-dominated shells, (Piran 1999), or reconnection events (Lyutikov 2006a). The afterglows, according to the fireball model, are generated in the external relativistic blast wave.

Since emission from the FS depends on "integrated properties" (total injected energy and total swept-up mass), the corresponding light curves were expected to be fairly smooth. In contrast, observations show the presence of unexpected features like flares and light-curve plateaus (Nousek et al. 2006; O'Brien et al. 2006; Gehrels & Razzaque 2013; Lien et al. 2016; de Pasquale et al. 2007; Chincarini et al. 2010; Mazaeva et al. 2018), abrupt endings of the plateau phases (Troja et al. 2007), fast optical variability (e.g., GRB 021004 and most notoriously GRB 080916C), missing (de Pasquale et al. 2016) and chromatic (Panaitescu 2007; Racusin et al. 2009) jet breaks, and missing RSs (Gomboc et al. 2009). These phenomena are hard to explain within the standard fireball model that postulates that the early X-ray are produced in the FS, as argued by Lyutikov (2009); Kann et al. (2010); and Lyutikov & Camilo Jaramillo (2017).

The origin of sudden drops in afterglow light curves is especially mysterious. For example, GRB 070110 starts with a normal prompt emission, followed by an early decay phase until approximately 100 and a plateau until $\sim 10^4$ s. At about 2×10^4 s, the light curve of the afterglow of GRB 070110 drops suddenly with a temporal slope >7 (Sbarufatti et al. 2007; Krimm et al. 2007a, 2007b; Troja et al. 2007).

Observations of early afterglows in long GRBs, at times $\leqslant 1$ day, require the presence of a long-lasting active central engine. Previously, some of the related phenomenology was attributed to a long-lasting central engine (see Section 2 for a more detailed discussion of various models of the long-lasting central engine). A number of authors have discussed a long-lasting engine that produces colliding shells, in analogy with the fireball model for prompt emission (Rees & Meszaros 1994; Panaitescu et al. 2006; Uhm & Beloborodov 2007; Barkov & Komissarov 2010; Barkov & Pozanenko 2011). The problem with this explanation is that energizing the FS requires a lot of energy: the total energy in the blast needs to increase linearly with time, hence putting exceptional demands on the efficiency of prompt emission (Panaitescu et al. 2006; Oates et al. 2007; de Pasquale et al. 2009). In addition, to producing afterglow flares in the FS the total energy in the explosion needs to roughly double each time: hence, the total energy grows exponentially for bursts with multiple flares.

As an alternative, Lyutikov & Camilo Jaramillo (2017) developed a model of early GRB afterglows with dominant X-ray contribution from the RS propagating in a highly relativistic (Lorentz factor $\gamma_w \sim 10^4 - 10^6$) magnetized wind of a long-lasting central engine; we will refer to this types of model as a "pulsar paradigm," stressing similarities to the physics of pulsar winds.

Pulsar wind nebulae are efficient in converting the spindown energy of the central objects, coming out in a form of the wind, into high energy radiation, reaching efficiencies of tens of percent (e.g., Kennel & Coroniti 1984a; Kargaltsev & Pavlov 2008). This efficiency is much higher than what would be expected from simple sigma scaling of dissipation at relativistic shocks (Kennel & Coroniti 1984b). The effects of magnetic dissipation contribute to higher efficiency (Sironi & Spitkovsky 2011; Porth et al. 2014).

Lyutikov & Camilo Jaramillo (2017) adopted the pulsar-wind model to the case of preceding expanding GRB shock. The model reproduces, in a fairly natural way, the overall trends and yet allows for variations in the temporal and spectral evolution of early optical and X-ray afterglows. The high energy and the optical synchrotron emission from the RS particles occurs in the fast-cooling regime; the resulting synchrotron power L_s is a large fraction of the wind luminosity (high-sigma termination shocks propagate faster through the wind, boosting the efficiency).

Thus, plateaus—parts of afterglow light curves that show slowly decreasing spectral power—are a natural consequence of the RS emission. Contribution from the FS is negligible in the X-rays, but in the optical both the FS and RS contribute similarly (but see, e.g., Warren et al. 2017, 2018; Ito et al. 2019): the FS optical emission is in the slow-cooling regime, producing smooth components, while the RS optical emission is in the fast-cooling regime, and thus can both produce optical plateaus and account for fast optical variability correlated with the X-rays, e.g., due to changes in the wind properties. The later phases of a pulsar-wind interaction with a supernova remnant are discussed by Khangulyan et al. (2018).

The goal of the present work is twofold. First, we perform a number of numerical simulations for the propagation of a highly relativistic magnetized wind that follows a relativistic shock wave. Previously, this problem was considered analytically by Lyutikov (2017). Second, we perform radiative calculations of the early X-ray afterglow emission coming from the ultrarelativistic RS of a long-living central engine. We demonstrate that this paradigm allows us to resolve the problems of plateaus, sudden intensity drops, and flares. Qualitatively, at early times, a large fraction of the wind power is radiated: this explains the plateaus. If the wind terminates, so that the emission from the RS ceases instantaneously, it leads to a sharp decrease in observed flux (since the particles are cooling fast). Finally, variations of the wind intensity can produce flares that bear resemblance to the ones observed in GRBs.

We argue in this paper that abrupt declines in afterglow curves can be explained if emission originates in the ultrarelativistic and highly magnetized RS of a long-lasting engine. Lyutikov & Camilo Jaramillo (2017) (see also Lyutikov 2017) developed a model of early GRB afterglows with dominant X-ray contribution from the highly magnetized ultrarelativistic RS, an analog of the pulsar-wind termination shock. The critical point is that emission from the RS in highly magnetized pulsar-like wind occurs in the fast-cooling regime. Thus, it reflects *instantaneous* wind power, not accumulated mass/energy, as in the case of the FS. Thus, it is more natural to produce fast variation in the highly magnetized RS.

2. Models of Long-lasting Winds in GRBs

The model of Lyutikov & Camilo Jaramillo (2017), explored in more detail here, differs qualitatively from a number of previous works that advocated for a long-lasting central engine in GRBs. Previous works can be divided into two categories. First, the type of model involving modifying the properties of the FS (e.g., re-energizing of the FS by the long-lasting wind in an attempt to produce flares; Rees & Mészáros 1998; Dai & Lu 1998; Panaitescu et al. 1998; Dai 2004). The second type of model assumes a long-lasting central engine that produces mildly relativistic matter-dominated winds (Sari & Piran 1999; Genet et al. 2007; Uhm & Beloborodov 2007; Komissarov & Barkov 2009; Uhm et al. 2012; Hascoët et al. 2017). In these types of models the emission is produced in a way similar to the internal shock model for the prompt emission (that is, collision of baryon-dominated shells, amplification of magnetic field, and particle acceleration).

The FS-based models encounter a number of fundamental problems (Lyutikov 2009; Uhm & Beloborodov 2007; though see Lyons et al. 2010; Rowlinson et al. 2010; Resmi & Zhang 2016; Beniamini & Mochkovitch 2017; Rowlinson et al. 2013; van Eerten 2014; Khangulyan et al. 2020; Warren et al. 2021). The key problem is that the properties of the FS are "cumulative," in the sense that its dynamics depend on the *total* swept-up mass and injected energy, which is impossible to change on a short timescale. For example, to produce a flare within the FS model, the total energy of the shock should increase substantially (e.g., by a factor of 2). To produce another flare, even more energy needs to be injected, leading to the exponentially increasing total energy with each flare.

Most importantly, the FS-based models cannot produce abrupt steep decays. Such sharp drops require (at the least) that the emission from the FS switch off instantaneously, however, this is impossible. First, the microphysics of shock acceleration is not expected to change rapidly (at least we have no arguments as to why it should).

Second, the variations of the hydrodynamic properties of the FS, as they translate to radiation, are also expected to produce smooth variations (Gat et al. 2013). As an example, consider a relativistic shock that breaks out from a denser medium (density n_1) into the less dense one (density $n_2 \ll n_1$). In the standard fireball model total synchrotron power P_s per unit area of the shock scale as (Piran 2004)

$$\begin{aligned} &P_s \propto n\Gamma^2\gamma'^2 B'^2 \propto n^2\Gamma^6 \\ &\gamma' \propto \Gamma \\ &B' \propto \Gamma\sqrt{n}, \end{aligned} \tag{1}$$

where Γ is the Lorentz factor of the shock, and γ' is the Lorentz factor of accelerated particles.

Importantly, if a shock breaks out from a dense medium into the rarefied one, with $n_2 \ll n_1$, it *accelerates* to approximately $\Gamma_2 \approx \Gamma_1^2$, as the post-shock internal energy in the first medium is converted into bulk motion (Johnson & McKee 1971; Lyutikov 2010). Thus, a change in power and peak frequency scale as

$$\frac{P_{s,2}}{P_{s,1}} = \Gamma_1^6\left(\frac{n_2}{n_1}\right)^2. \tag{2}$$

Thus, even though we assumed $n_2 \ll n_1$, the synchrotron emissivity in the less dense medium is largely compensated by the increase of the Lorentz factor. Since the expected Lorentz factor at the time of sharp drops is $\Gamma_1 \sim$ few tens, suppression of emission from the FS requires the unrealistically large decrease of density.

Oganesyan et al. (2020) discussed the appearance of plateaus from an off-axis jet (so that a more energetic part of the FS becomes visible and effectively boosts the observed flux. We expect though that at observer times of a few $\times 10^4$ s the X-ray emitting particles in the FS are in the slow-cooling regime, liming how short timescales in the observed emission light curves can be produced.

The model of Lyutikov & Camilo Jaramillo (2017) and the present investigation are more aligned with the previously discussed emission from the RS (Sari & Piran 1999; Genet et al. 2007; Uhm & Beloborodov 2007; Uhm et al. 2012; Hascoët et al. 2017). But the present model is qualitatively different: the emission properties here are parameterized within the pulsar-wind paradigm of Kennel & Coroniti (1984a), not the fireball model (e.g., Piran 2004). Qualitatively, the advantage of the present model of the highly magnetized/highly relativistic RS emission over the fireball adaptation to the RS case are similar to the prompt emission: highly magnetized relativistic flows can be more efficient in converting the energy of the explosion to radiation, as they do not "lose" energy on the bulk motion of non-emitting ions (Lyutikov & Blandford 2003; Lyutikov 2006a).

The pulsar-wind paradigm of Kennel & Coroniti (1984a) also has a very different prescription for particle acceleration and emission: it relates the typical (minimum) Lorentz factor of the accelerated particles to the Lorentz factor of the pre-shock wind $\gamma_{\min} \sim \gamma_w$ with $\gamma_w \sim 10^4$–10^6), while the magnetic field in the emission region follows the shock compression relations. In contrast, the fireball model parameterizes both the Lorentz factor of the accelerated particles and the (shock-amplified) magnetic field to the upstream properties of the baryon-dominated energy flow (e.g., $\gamma_{\min} \sim \epsilon_e (m_p/m_e)\gamma_w$ with $\gamma_w \sim 10^2$). The resulting emission properties are qualitatively different.

3. Relativistic Double Explosion

3.1. Triple-shock Structure

Consider the relativistic point explosion of energy E_1 in a medium with constant density $\rho_{\rm ex} = m_p n_{\rm ex}$, followed by a wind with constant luminosity L_w (Lyutikov 2017, both E_1 and L_w are isotropic equivalent values). The initial explosion generates a Blandford–McKee forward shock wave (BMFS; Blandford & McKee 1976)

$$\begin{aligned}
\Gamma_1 &= \sqrt{\frac{17}{8\pi}}\sqrt{\frac{E_1}{\rho_{\rm ex} c^5}}\, t^{-3/2}\\
p_1 &= \frac{2}{3}\rho_{\rm ex} c^2 \Gamma_1^2 f_1(\chi)\\
\gamma_1^2 &= \frac{1}{2}\Gamma_1^2 g_1(\chi)\\
n_1 &= 2 n_{\rm ex}\Gamma_1 n_1(\chi)\\
f_1(\chi) &= \chi^{-17/12}\\
g_1(\chi) &= 1/\chi\\
n_1(\chi) &= \chi^{-5/4}\\
\chi &= [1 + 2(m+1)\Gamma^2](1 - r/t). \qquad (3)
\end{aligned}$$

Subscript *ex* indicates the properties in the surrounding medium; subscript 1 indicates that quantities are measured behind the leading BMFS; hence, between the two FSs. The Lorentz factor Γ depends on time as $\Gamma^2 \propto t^{-m}$, $m = 3$.

We assume that the initial GRB explosion leaves behind an active remnant—a black hole or (fast-rotating) neutron star. The remnant produces a long-lasting pulsar-like wind, either using the rotational energy of the newly born neutron star (Usov 1992; Komissarov & Barkov 2007), accretion of the pre-explosion envelope onto the black hole (Cannizzo & Gehrels 2009), or if the black hole can keep its magnetic flux for a sufficiently long time (Komissarov & Barkov 2009; Barkov & Komissarov 2010; Lyutikov 2011; Lyutikov & McKinney 2011).

One expects that the central engine produces very fast and light wind that will start interacting with the slower, but still relativistically expanding, ejecta. As the highly relativistic wind from the long-lasting engine interacts with the initial explosion, it launches a second FS in the medium already shocked by the primary blast wave. At the same time, the RS forms in the wind; the two shocks are separated by the contact discontinuity (CD), Figure 1.

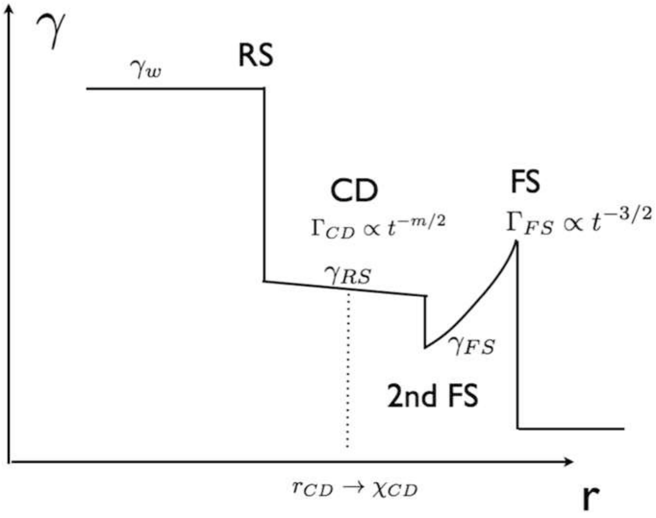

Figure 1. Velocity structure of the triple-shock configuration. Leading is the FS that generates a self-similar post-shock velocity and pressure profile. A fast wind with Lorentz factor γ_w is terminated at the RS; the post-RS flow connects through the CD (dotted line) to the second shock driven in the already shocked media. The CD is located at $r_{\rm CD}$, corresponding to $\chi_{\rm CD}$. The RS and the second forward shock (2nd FS) are located close to $\chi_{\rm CD}$ (Lyutikov & Camilo Jaramillo 2017).

First, we assume that external density is constant, while the wind is magnetized with constant luminosity (variations in wind luminosity are explored in Section 5)

$$L_w = 4\pi\gamma_w^2\left(\rho_w c^2 + \frac{B_w^2}{4\pi}\right) r^2 c, \qquad (4)$$

where ρ_w and B_w are the density and magnetic field measured in the wind rest frame. Thus,

$$B_w = \sqrt{\frac{\sigma_w}{1+\sigma_w}}\sqrt{\frac{L_w}{c}}\frac{1}{r\gamma_w}, \qquad (5)$$

where

$$\sigma_w = \frac{B_w^2}{4\pi\rho_w c^2} \qquad (6)$$

is the wind magnetization parameter (Kennel & Coroniti 1984b). In our pulsar-wind paradigm, we assume that the mass loading of the wind is very small, while the the wind is assumed to be very fast, with $\gamma_w \gg \Gamma_{\rm FS}, \Gamma_{\rm CD}$.

3.2. Analytical Expectations: Self-similar Stages

Generally, the structure of the flows in double explosions is non-self-similar (Lyutikov 2017). First, with time the second FS approaches the initial FS; for sufficiently powerful winds the second FS may catch up with the primary FS. The presence of this special time violates the assumption of self-similarity. We can estimate the catch-up time by noticing that the power deposited by the wind in the shocked medium scales as $L_w/\Gamma_{\rm CD}^2$. Thus, in coordinate time the wind deposits energy similar to the initial explosion at the time when $\Gamma_{\rm CD} \sim \Gamma_{\rm FS}$,

$$\begin{aligned} t_{\rm eq} &= \Gamma_{\rm FS}^2 \frac{E_1}{L_w} \propto \left(\frac{E_1^2}{c^5 \rho L_w}\right)^{1/4} \\ &= 2 \times 10^7\, E_{1,52}^{1/2},\, L_{w,46}^{-1/4} n^{-1/4} {\rm s}, \end{aligned} \tag{7}$$

almost a year in coordinate time. At times $t \leqslant t_{\rm eq}$ the second shock is approximately self-similar, the CD is located far downstream of the first shock, and is moving with time in the self-similar coordinate χ, associated with the primary shock, toward the first shock. The motion of the first shock is unaffected by the wind at this stage. At times $t \geqslant t_{\rm eq}$, the two shocks merge—the system then relaxes to a Blandford & McKee (BM; 1976) self-similar solution with energy supply.

In the numerical estimate in Equation (7) we used the wind power $L_w \sim 10^{46}$ erg s^{-1}, which at first glance may look too high. Indeed, the total energy budget for isotropic wind is then $E_w \sim L_w t_{\rm eq} \sim 10^{53}$ erg, and this value is a much larger rotating energy of a fast spinning NS $\sim 10^{52}$ erg. But recall that this is an isotropic equivalent power. In the case of long GRBs, both the initial explosion and the power of the long-lived central engine are collimated into small angle $\theta \sim 0.1$ rad (e.g., Komissarov & Barkov 2007). After jet-break out the opening angle remains nearly constant. Thus, the true wind power can be estimated as $L_{w,\rm true} \approx \theta^2 L_w/2 \sim 10^{44}$ erg s^{-1} and $E_w \sim 10^{51}$ erg, which is an allowed energy budget of fast spinning neutron star.

Second, the self-similarity may be violated at early times if there is an effective delay time t_d between the initial explosion and the start of the second wind. (This issue is also important in our implementation scheme, Section 4—since we start the simulation with energy injection at some finite distance from the primary shock this is equivalent to some effective time delay for the wind turn-on.)

Suppose that the secondary wind turns on at time t_d after the initial one and the second shock/CD is moving with the Lorentz factor

$$\Gamma_{\rm CD}^2 \propto (t - t_d)^{-m}. \tag{8}$$

Then, the location of the second shock at time t is

$$R_{\rm CD} = (t - t_d)\left(1 - \frac{1}{2\Gamma_{\rm CD}^2 (m+1)}\right). \tag{9}$$

The corresponding self-similar coordinate of the second shock in terms of the primary shock self-similar parameter χ is

$$\begin{aligned} \chi_{\rm CD} &= (1 + 8\Gamma_1^2)\left(1 - \frac{R}{t}\right) \\ &\approx \left(\frac{8 t_d}{t} + \frac{4}{(m+1)\Gamma_{\rm CD}^2}\right)\Gamma_1^2. \end{aligned} \tag{10}$$

The effective time delay t_d introduces additional (besides the catch-up time, Equation (7)) timescales in the problem. Thus, even within the limits of the expected self-similar motion, $t \ll t_{\rm eq}$ the effective delay time t_d violates the self-similarity assumption. Still, depending on whether the ratio $t_d/(t\Gamma_{\rm CD}^2)$ is much larger or smaller than unity, we expect approximately self-similar behavior (Lyutikov 2017; Lyutikov & Camilo Jaramillo 2017)

For $t_d \geqslant t/(2(m+1)\Gamma_{\rm CD}^2)$, the location of the CD in the self-similar coordinate associated with the first shock is

$$\chi_{\rm CD} \approx \frac{8\gamma_1^2 t_d}{t} \propto t^{-4}, \tag{11}$$

$$\Gamma_{\rm CD} = 0.52 \frac{E_1^{5/48} t_d^{5/48} L_w^{1/4}}{c^{85/48} \rho^{17/48} t^{11/12}}. \tag{12}$$

Alternatively, for $t_d \leqslant t/(2(m+1)\Gamma_{\rm CD}^2)$,

$$\chi_{\rm CD} = 2.68 \left(\frac{E_1}{c^{5/2}\sqrt{\rho}\, t^2 \sqrt{L_w}}\right)^{24/29}, \tag{13}$$

$$\Gamma_{\rm CD} = 0.50 \frac{E_1^{5/58} L_w^{6/29}}{c^{85/58} \rho^{17/58} t^{39/58}}. \tag{14}$$

Finally, if the second explosion is pointlike with energy E_2, and the Lorentz factor of the second shock evolves according to Lyutikov (2017)

$$\gamma_2 = \sqrt{\frac{71}{2}} \left(\frac{17}{\pi}\right)^{5/24} \left(\frac{E_1^5 t_d^5}{c^{85} (m_p n_{\rm ex})^{17}}\right)^{1/24} \sqrt{E_2}\, t^{-7/3} \tag{15}$$

(this expression is applicable for $t \leqslant \Gamma_1^2 t_d$, the time when the second shock catches with the primary shock).

Relations (12)–(15) indicate that depending on the particularities of the setup, we expect somewhat different scalings for the propagation of the second shock (we are also often limited in integration time to see a switch between different self-similar regimes).

The point of the previous discussion is that mild variations between the properties of double explosions (delay times, luminosity of the long-lasting engine) are expected to produce a broad variety of behaviors, like various power-law indices and a temporarily change in overall behavior. This ability of the model to accommodate a fairly wide range of behaviors with a minimal numbers of parameters is important in explaining highly temporally variable early afterglows, as we further explore in this paper.

4. Numerical Simulations of Relativistic Double Explosions

4.1. Setup of the Simulations

The simulations were performed using a one-dimensional geometry in spherical coordinates using the PLUTO code[3] (Mignone et al. 2007). Spatial parabolic interpolation, a third order Runge–Kutta approximation in time, and a Harten–Lax–van Leer discontinuities Riemann solver were used (Mignone et al. 2009). PLUTO is a modular Godunov-type code entirely written in C and intended mainly for astrophysical applications and high Mach number flows in multiple spatial dimensions. The simulations were run through the Message Passing Interface library in the Deutsches Elektronen-Synchrotron (Germany) cluster. The flow has been approximated as an ideal, relativistic adiabatic gas with and without the toroidal magnetic field, one particle species, and a polytropic index of 4/3. The adopted resolution is 192,000 cells. The size of the domain is $r \in [0.95, 4] R_{\rm s}$ or $r \in [0.98, 4] R_{\rm s}$; here, $R_{\rm s}$ is the initial position of shock wave front.

As an initial condition we set the solution of BM with a shock radius of 1 and Equation (3), and the Lorentz factor of

---

[3] Link http://plutocode.ph.unito.it/index.html.

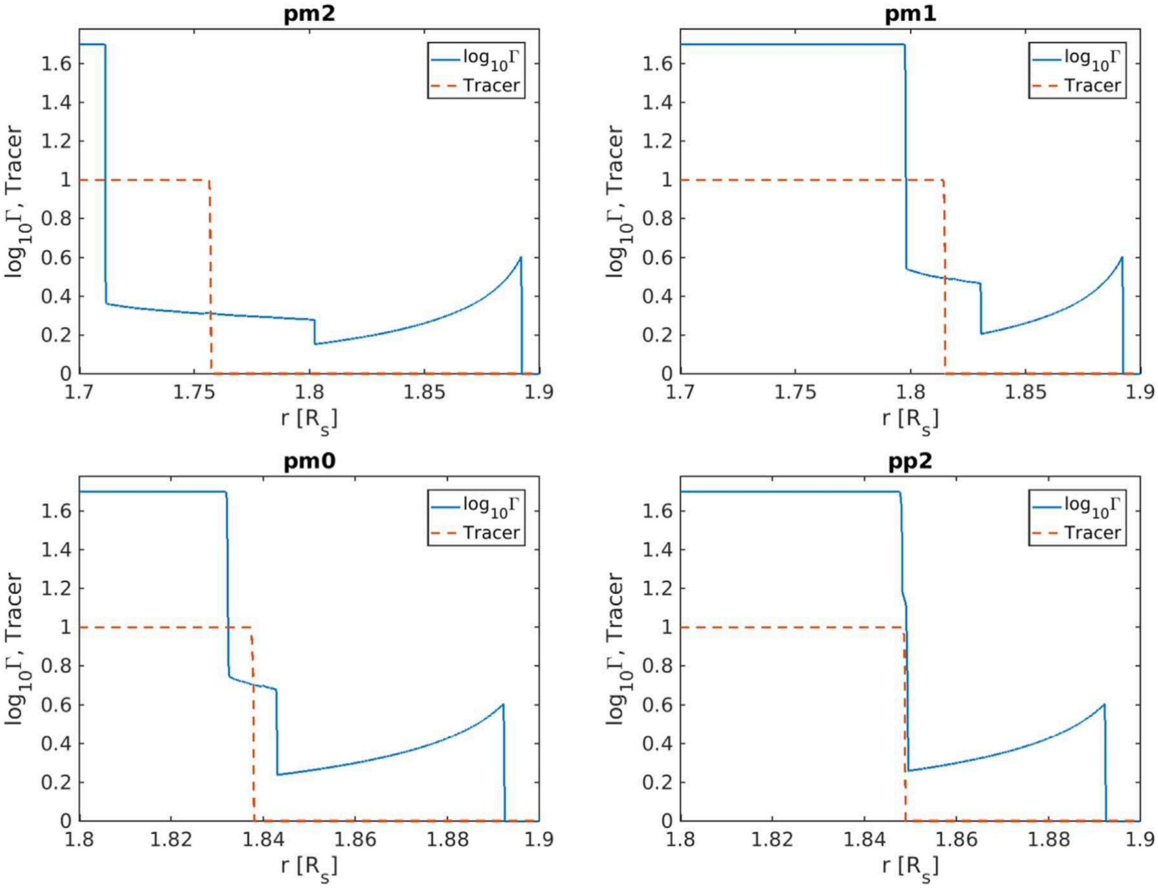

Figure 2. Hydrodynamic simulations of the double explosion. Plotted are the Lorentz factor and tracer distribution as a function of radius at the moment $t = 1.9$ $[r_s/c]$. The tracer distinguishes the wind from the shocked external medium. The parameters for each panel are encoded in the titles, Table 1.

the shock was 15. The external matter was assumed uniform with a density $\rho = 1$ and pressure $p = 10^{-4}$ (in units $c = 1$). The pressure and density just after the shock was determined by the BM solution ($\rho_{\rm BM} = 42.43$ and $p_{\rm BM} = 150$) with the total energy of $E_{\rm BM} = 2.13 \times 10^5$. From the left boundary (from the center) at radius $r_{\rm w} = 0.95$ or $r_{\rm w} = 0.98$ (models are marked by the letter "*s*" at the end of their names) was injected wind with an initial Lorentz factor of $\gamma_{\rm w} = 50$, and the pressure of the wind was fixed at $p_w = 10^{-3}\rho_w c^2$. The parameters of the models are listed in Table 1.[4]

The chosen setup corresponds to the following physical parameters: the density unit $n_{\rm ISM} = 1$ cm^{-3}, total isotropic explosion energy $E_{\rm ISO} = 1.5 \times 10^{52}$ erg, laboratory time $t_{\rm lab} = R_s/c = 10^7$ s, the initial radius of the shock $R_s = 3 \times 10^{17}$ cm, and observer time $t_{\rm obs} = 4.4 \times 10^3$ s. The isotropic wind power unit is $L_{w,0} = 1.2 \times 10^{47}$ erg s^{-1}.

We performed nine runs without magnetic field and eight runs with different magnetizations. Our numerical model for the primary shock is consistent with analytical solution of BM with an accuracy of ~10% (pressure, density, and maximal Lorentz factor). On the top of each panel of Figures 2–10 we indicate name of the model with the parameters presented in the Table 1.

Table 1
Parameters of the Models

Model	$\rho_{\rm w}$	$r_{\rm w}$	$\sigma_{\rm w}$	$L_{\rm w}$ $[L_{w,0}]$
*pm*4	10^{-4}	0.95	0	10^{-4}
*pm*3	10^{-3}	0.95	0	10^{-3}
*pm*2	10^{-2}	0.95	0	10^{-2}
*pm*2*s*	10^{-2}	0.98	0	10^{-2}
*pm*1	10^{-1}	0.95	0	10^{-1}
*pm*0	1	0.95	0	1
*pp*1	10^1	0.95	0	10^1
*pp*2	10^2	0.95	0	10^2
*pp*2*s*	10^2	0.98	0	10^2
*mm*1*p*1	10^1	0.95	0.1	11
*m*0*p*1	10^1	0.95	1.0	20
*m*05*p*1	10^1	0.95	3.0	40
*m*1*p*1	10^1	0.95	10	110
*mm*1*ep*1	9.09	0.95	0.1	10^1
*m*0*ep*1	5.00	0.95	1.0	10^1
*m*05*ep*1	2.50	0.95	3.0	10^1
*m*1*ep*1	0.91	0.95	10	10^1

4.2. Results: Long-term Dynamics of Double Explosions

4.2.1. Unmagnetized Secondary Wind

In the unmagnetized models labeled pXX, we vary the wind density. The wind density varies from 10^{-4} for the *pm4* model to 10^2 for *pp2*. In Figure (2) we plot the results of the pXX

---

[4] We change the wind density here, but the power of the wind can be varied by the wind Lorentz factor, magnetization, or pressure. The main ingredient will be the total energy flux.

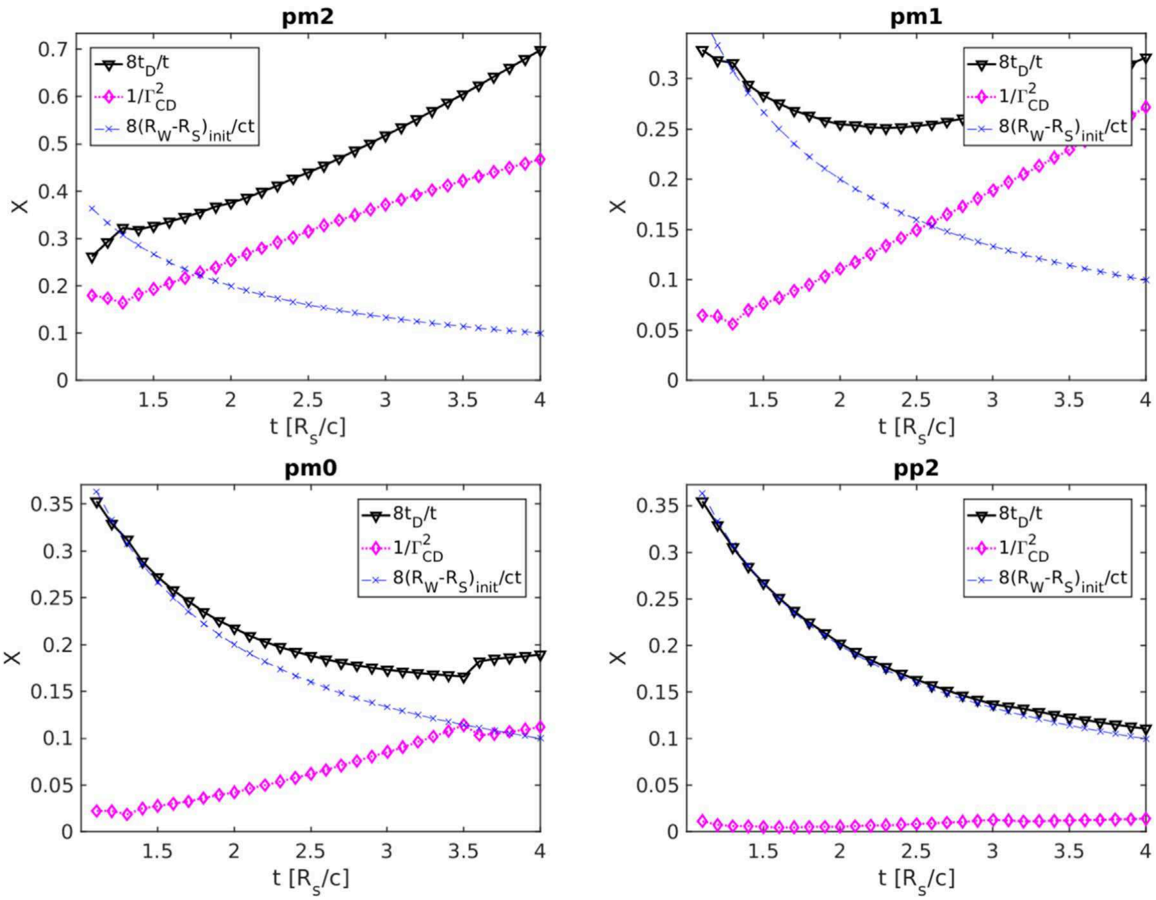

Figure 3. Self-similar coordinate of the second shock χ, Equation (10), as function of time for different models. Plotted are values of $8t_{\rm d}/t$ from simulation (triangles), analytical curve (crosses) (Lyutikov 2017). Also plotted is the square of inverse Lorentz factor (diamonds). Models with high wind power *pm*0 and *pp*2 closely follow the theoretical curve.

models where we vary the power of the hydrodynamical wind. At small radius one can clearly identify the location of the RS, where the Lorentz factor suddenly drops. At larger radius the CD is identified by the the position of the tracer drop. Further out is the secondary forward shock, and the initial BM shock. More curves can be seen in the Appendix A.1.

In Figure 3, three curves are shown for the pXX models: (i) theoretical curve based on the expectation from the initial conditions $t_{\rm d} = (r_{\rm s} - r_{\rm w})/c$; (ii) inverse square of the Lorentz factor; (iii) actual time of delay calculated from position of the CD and its Lorentz factor using Equation (10). As we can see in the models *pm*0, *pp*1, and *pp*2 (power of the wind comparable to initial explosion) the theoretical and actual curves are close. More powerful wind ($L_{\rm w} r_{\rm s}/c \geqslant 0.1 E_{\rm BM}$) can push the CD much faster, which allows satisfying conditions (8). Large value of $\Gamma_{\rm CD}$ also relax the applicability condition of (12). So, a similar picture can be seen as shown in Figure 4, where models *pp*2, *pp*1, and *pm*0 follow the theoretically predicted time dependence (see Equation (12)) $\Gamma_{\rm CD} \propto t^{-11/12}$. Deviations from the theoretical curves in Figures 3 and 4 at late time are due to the fact that the wind-triggered FS reach the radius of the BMFS, affecting the motion of the initial shock: in this case, the transition to a wind-driven BM solution occurs. The Lorentz factor is fitted by the power law $\Gamma_{\rm CD} \propto t^{-0.45}$.

Figure 5 shows the time dependence of the Lorentz factor at the CD and its $\chi_{\rm CD}$. For high relative wind power, the slope of the Lorentz factor coincides with the theoretical one. Moreover, the dependence of the theoretical Lorentz factor on wind power (see Equation (12)) $\Gamma_{\rm CD} \propto L_{\rm w}^{0.25}$ and the simulated one (Figure 6) $\Gamma_{\rm CD} \propto L_{\rm w}^{0.18}$) are in a good agreement.

The time behavior of the theoretically predicted $\chi_{\rm CD}$ ($\chi_{\rm CD} \propto t^{\alpha_\chi}$, $\alpha_\chi = -4$) is in a good agreement with the models with high relative wind power, see Figures 7 and 8, which show a tendency of the power slope to $\alpha_\chi = -3.8$ at large wind powers. After the moment that the wind-driven FS reaches the BMFS, the slope is changed and tends to $\alpha_\chi = -2.7$.

The deviation from the theoretically predicted slope $\Gamma_{\rm CD} \propto t^{-0.92}$ takes place when the wind power is low. The low power wind forms a sub-relativistic shock, which pushes the sub-relativistic CD. Since the analytic theory is applicable in the ultrarelativistic regime, this explains the deviations of the numerical results from theory for $\Gamma_{\rm CD} < 3$. The same effect works for the dependence of $\chi_{\rm CD}$ on time. Sub-relativistic motion of CD can only have small values of $\alpha_\chi \sim -2$, and powerful winds in the relativistic regime show good agreement with theoretical predictions.

4.2.2. Magnetized Secondary Wind

Magnetized models marked as mXXp1 have a constant wind density, where XX indicates the magnetization of the flow. Magnetized models marked as mXXep1 have a constant wind

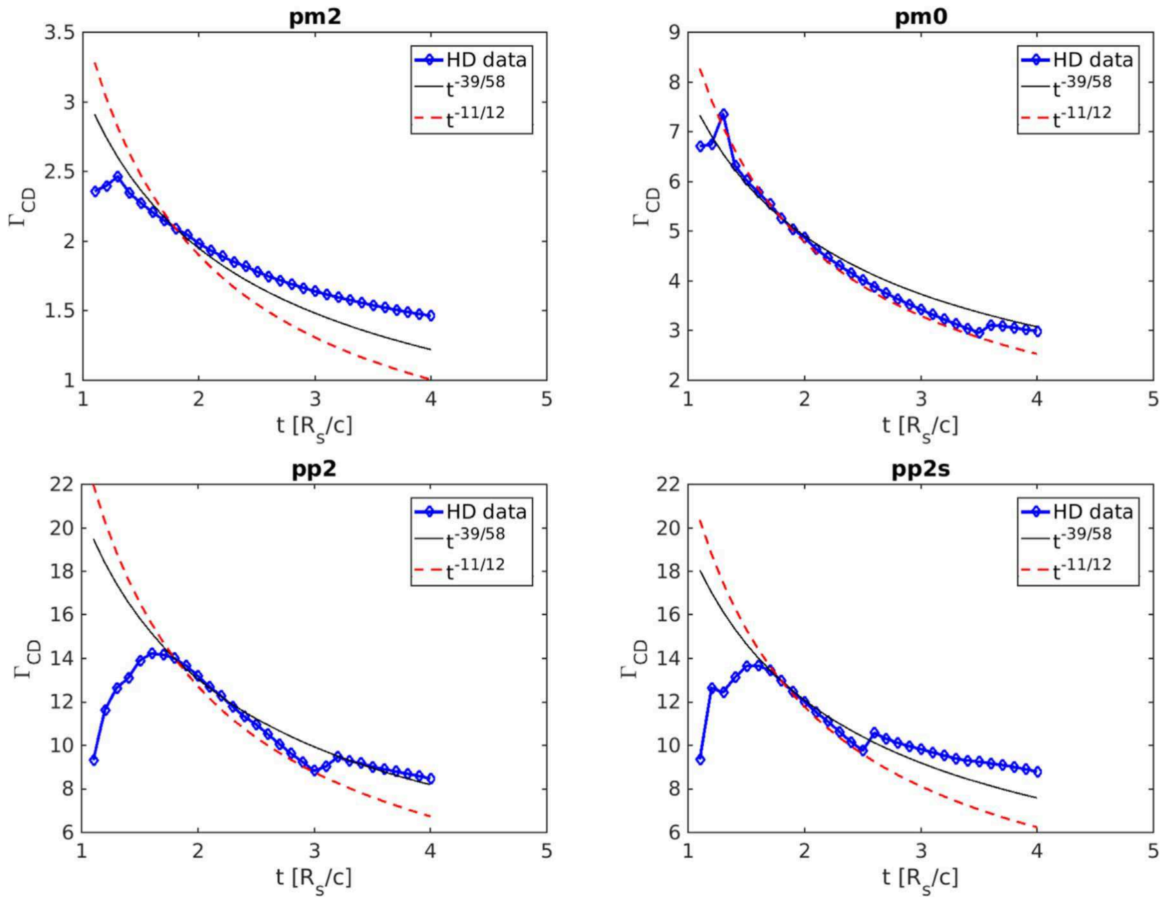

Figure 4. Lorentz factor of the CD as function of time—triangles and analytical expectations (Lyutikov 2017). The jumps in the Lorentz factor at later times occurs when the wind-driven FS catches up with the leading BMFS.

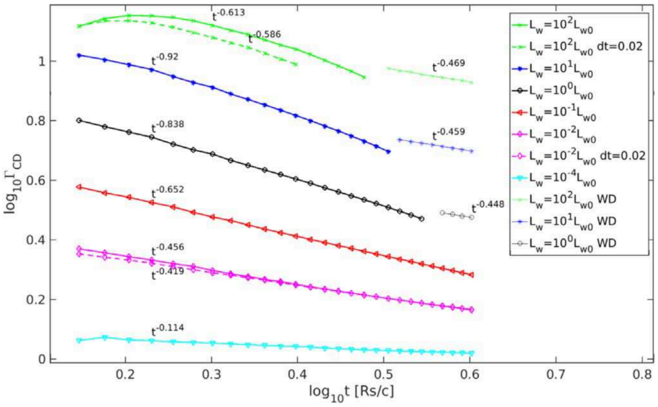

Figure 5. Lorentz factor of CD as a function of time . The analytical estimations (see Equation (12)) $\Gamma_{\rm CD} \propto t^{-0.92}$ and for wind-driven shock $\Gamma_{\rm CD} \propto t^{-0.5}$ (see thin lines with crosses, stars and circles). We calculate the power indexes on the straight parts of the curves, $\log_{10} t > 0.3$.

luminosity, where XX indicates the magnetization of the flow. As a basis for the magnetized wind models, we chose the model *pp*1, which has $L_{\rm w} r_{\rm s}/c \approx E_{\rm BM}$, so that the total wind power injected during the simulation is compatible to the energy of the initial explosion. Figure (9) illustrates the structure of the solution. The main difference between the unmagnetized models is that the thickness of a layer between the FS and RS increases with magnetization, and a similar conclusion was reached by Mimica et al. (2009). This is related to a decrease in the compressibility of the magnetized matter. Also note, that in models with a similar total power of the wind, the position of the FS is almost independent of magnetization, while the position of the RS strongly depends on the wind magnetization, the RS moves slower in highly magnetized models. More profiles of the solutions can be found in the Appendix A.2.

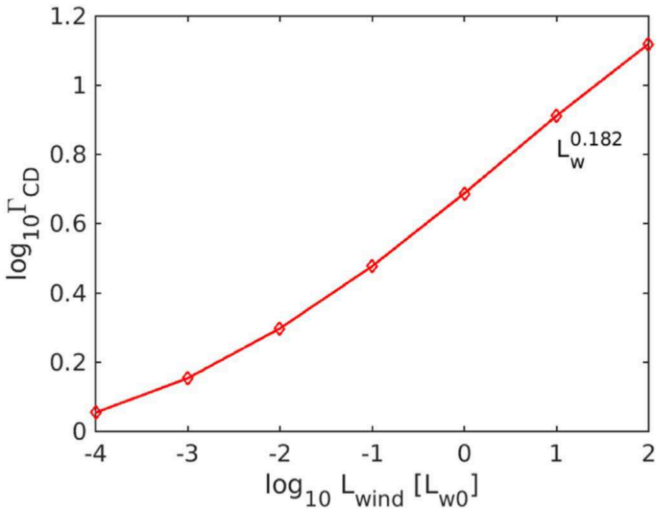

Figure 6. Dependence of the Lorentz factor of the CD at $t = 2[R_{\rm s}/c]$. In the high wind power regime the scaling is close to the expected $\Gamma_{\rm CD} \propto L_w^{1/4}$, Equation (12).

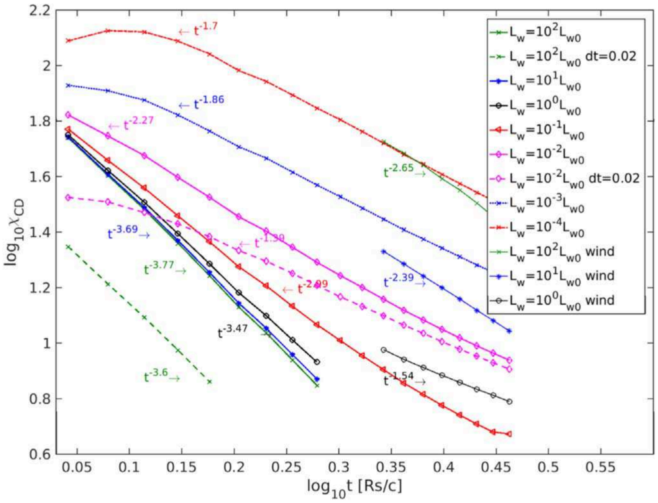

Figure 7. Time dependence of the $\chi_{\rm CD}$ of the CD. We calculate the power indexes on the straight parts of the curves, $\log_{10} t > 0.2$.

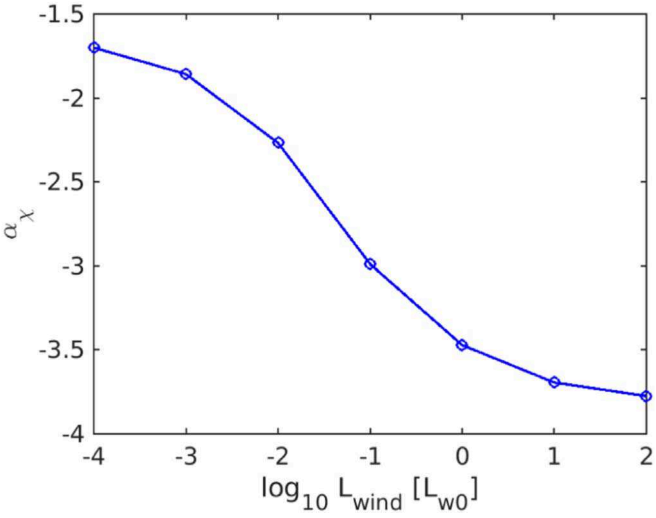

Figure 8. Dependence of the power slope α_χ at $t = 2[R_s/c]$.

All of the magnetized wind models show good agreement between the theoretical expectation $t_{\rm d}$ and the actual ones, see Figure 10. The Lorentz factor of the CD is also nicely fitted by the theoretical curve (Equation (12)).

The power of the slope of Lorentz factor of the CD is in good agreement with the theoretical one for the wind independent of its magnetization, see Figure 11. Moreover, the Lorentz factor of the CD very weakly depends on magnetization. If the power of the wind is conserved, $\Gamma_{\rm CD} \propto \sigma_{\rm w}^{0.023}$, and we preserve the hydrodynamical part of the flow and increase the magnetization trough increasing the magnetic flux, we get $\Gamma_{\rm CD} \propto \sigma_{\rm w}^{0.18}$, which is similar to the response of the $\Gamma_{\rm CD}$ with the increase in wind power.

The power slope of the time dependence of $\chi_{\rm CD}$, $\alpha_{\rm CD}$ (see Figure 12) almost does not depend on wind magnetization (Figure 13), and its value is close to the theoretically predicted slope of -4.

5. Emission from Relativistic Termination Shock: Flares, Plateaus, and Steep Decays

Next, we perform analytical calculations of the expected emission properties of highly magnetized RSs. We assume that particles are accelerated at the RS, and then experience radiative and adiabatic decays. In Section 5.1, we calculate the evolution of the distribution function for particles injected at the shock. The general relations for the observed intensity are calculated in Section 5.2.

5.1. Evolution of the Distribution Function

As discussed above, the dynamics of the second shock depends on the internal structure of the post-first-shock flow and the wind power; all relations are highly complicated by the relativistic and time-of-flight effects. To most clearly demonstrate the essential physical effects, we assume a simplified dynamics of the second shock, allowing it to propagate with constant velocity. Thus, in the frame of the shock, the magnetic field decreases linearly with time,

$$B' = B_0' \frac{t_0'}{t'}, \tag{16}$$

where time t_0' and magnetic field B_0' are some constants. In the following, we assume that the RS starts to accelerate particles at time t_0', and we calculate the emission properties of the particles injected at the wind termination shock, taking into account radiative and adiabatic losses.

As the wind generated by the long-lasting engine starts to interact with the tail part of the flow generated by the initial explosion, the RS forms in the wind, see Figure 1. Let us assume that the RS accelerates particles with a power-law distribution,

$$f(\gamma', t_i') \propto \gamma'^{-p} \Theta(\gamma' - \gamma'_{\rm min}), \tag{17}$$

where t_i' is the injection time, Θ is the step function, γ' is the Lorentz factor of the particles, and $\gamma'_{\rm min}$ is the minimum Lorentz factor of the injected particles; primed quantities are measured in the flow frame. The minimal Lorentz factor $\gamma'_{\rm min}$ can be estimated as (Kennel & Coroniti 1984a)

$$\gamma'_{\rm min} \sim \gamma_{\rm RS} \sim \gamma_w / 2\Gamma_{\rm RS}. \tag{18}$$

We stress that in the pulsar-wind paradigm the minimal Lorentz factor of accelerated particles $\gamma'_{\rm min}$ scales differently from the matter-dominated fireball case, where it is related to a fraction of baryonic energy ϵ_e carried by the wind, e.g., Sari et al. (1998).

The accelerated particles produce synchrotron emission in the ever-decreasing magnetic field, while also experiencing adiabatic losses. Synchrotron losses are given by the standard relations (e.g., Lang 1999). To take into account the adiabatic losses, we note that in a toroidally dominated case, the conservation of the first adiabatic invariant (constant magnetic flux through the cyclotron orbit) gives

$$\partial_{t'} \ln \gamma' = \frac{1}{2} \partial_{t'} \ln B'. \tag{19}$$

Thus, we assume that that the magnetic field is dominated by the large-scale toroidal field.

Using Equation (16) for the evolution of the field, the evolution of a particles' Lorentz factor follows

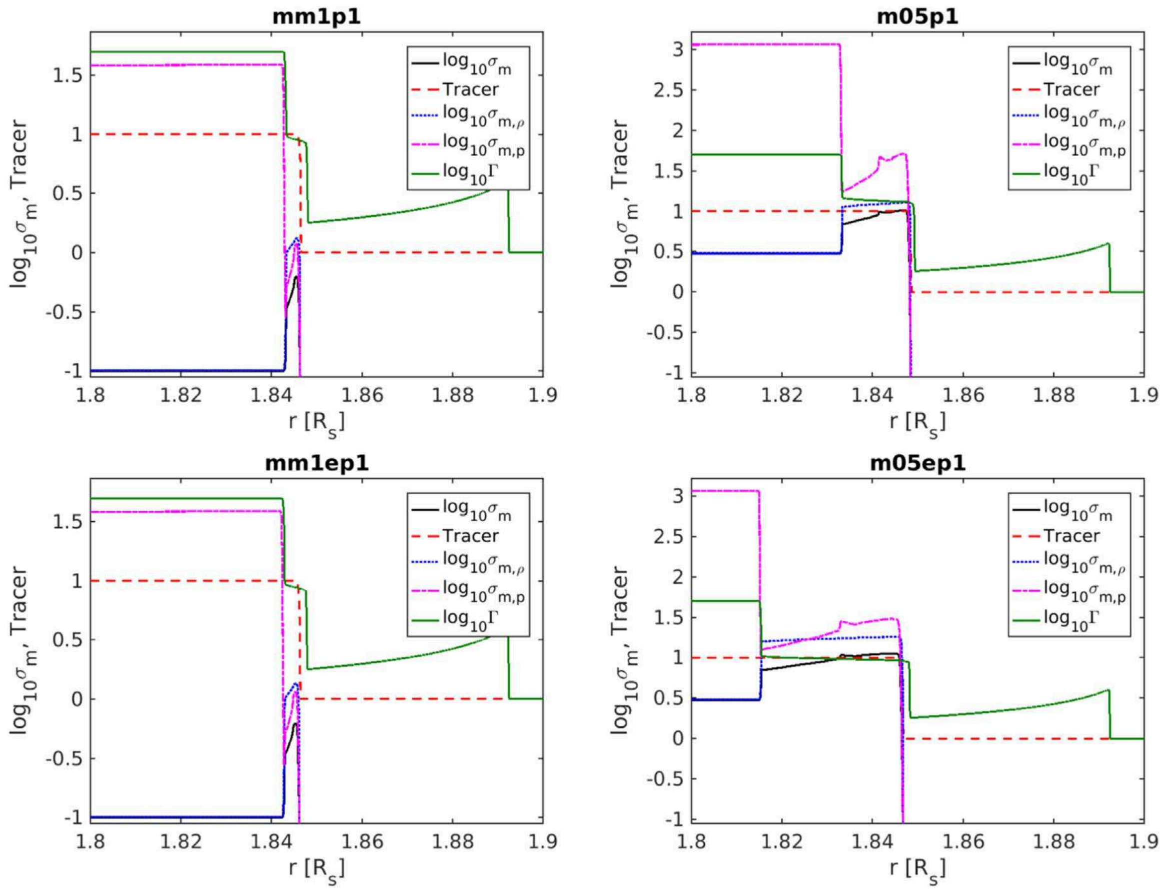

Figure 9. Magnetization, tracer, and Lorentz factor distribution for the magnetized models. As theory predicts, the thickness of the RS region increases with magnetization.

$$\frac{d\gamma'}{dt'} = -\frac{\tilde{C}_1 B_0'^2 \gamma'^2}{t'^2} - \frac{\gamma'}{2t'}$$
$$\tilde{C}_1 = \frac{\sigma_T t_0'^2}{6\pi m_e c}, \tag{20}$$

where σ_T is the Thomson cross section and t_0' is some reference time.

Solving for the evolution of the particles' energy in the flow frame,

$$\frac{1}{\gamma'} = \frac{2\tilde{C}_1 B_0'^2}{3t'}\left(\left(\frac{t'}{t_i'}\right)^{3/2} - 1\right) + \frac{1}{\gamma_i'}\sqrt{\frac{t'}{t_i'}}, \tag{21}$$

we can derive the evolution of a distribution function (the Green's function) (e.g., Kardashev 1962; Kennel & Coroniti 1984a)

where $\gamma_{\rm low}'$ is a lower bound of the Lorentz factor due to the minimum Lorentz factor at the injection, and $\gamma_{\rm up}'$ is an upper bound of the Lorentz factor due to cooling.

Once we know the evolution of the distribution function injected at time t_i', we can use the Green's function to derive the total distribution function by integrating over the injection times

$$N(\gamma', t') \propto \int_{t_i'}^{t'} \dot{n}(t_i') G(\gamma', t', t_i') dt_i', \tag{23}$$

where $\dot{n}(t_i')$ is the injection rate (assumed to be the constant below).

5.2. Observed Intensity

The intensity observed at each moment depends on the intrinsic luminosity, the geometry of the flow, and the relativistic and

$$G(\gamma', t', t_i') = \begin{cases} \gamma'^{-p}\left(\frac{t_i'}{t'}\right)^{\frac{p-1}{2}}\left(1 - \frac{2}{3}\tilde{C}_1 B_0'^2 \gamma_w' \sqrt{t'}\left(\frac{1}{t_i'^{3/2}} - \frac{1}{t'^{3/2}}\right)\right)^{p-2}, & \gamma_{\rm low}' < \gamma' < \gamma_{\rm up}' \\ 0, & \text{else} \end{cases}$$
$$\frac{1}{\gamma_{\rm low}'} = \frac{2\tilde{C}_1 B_0'^2}{3t'}\left(\left(\frac{t'}{t_i'}\right)^{3/2} - 1\right) + \frac{1}{\gamma_{\rm min}'}\sqrt{\frac{t'}{t_i'}}$$
$$\frac{1}{\gamma_{\rm up}'} = \frac{2\tilde{C}_1 B_0'^2}{3t'}\left(\left(\frac{t'}{t_i'}\right)^{3/2} - 1\right), \tag{22}$$

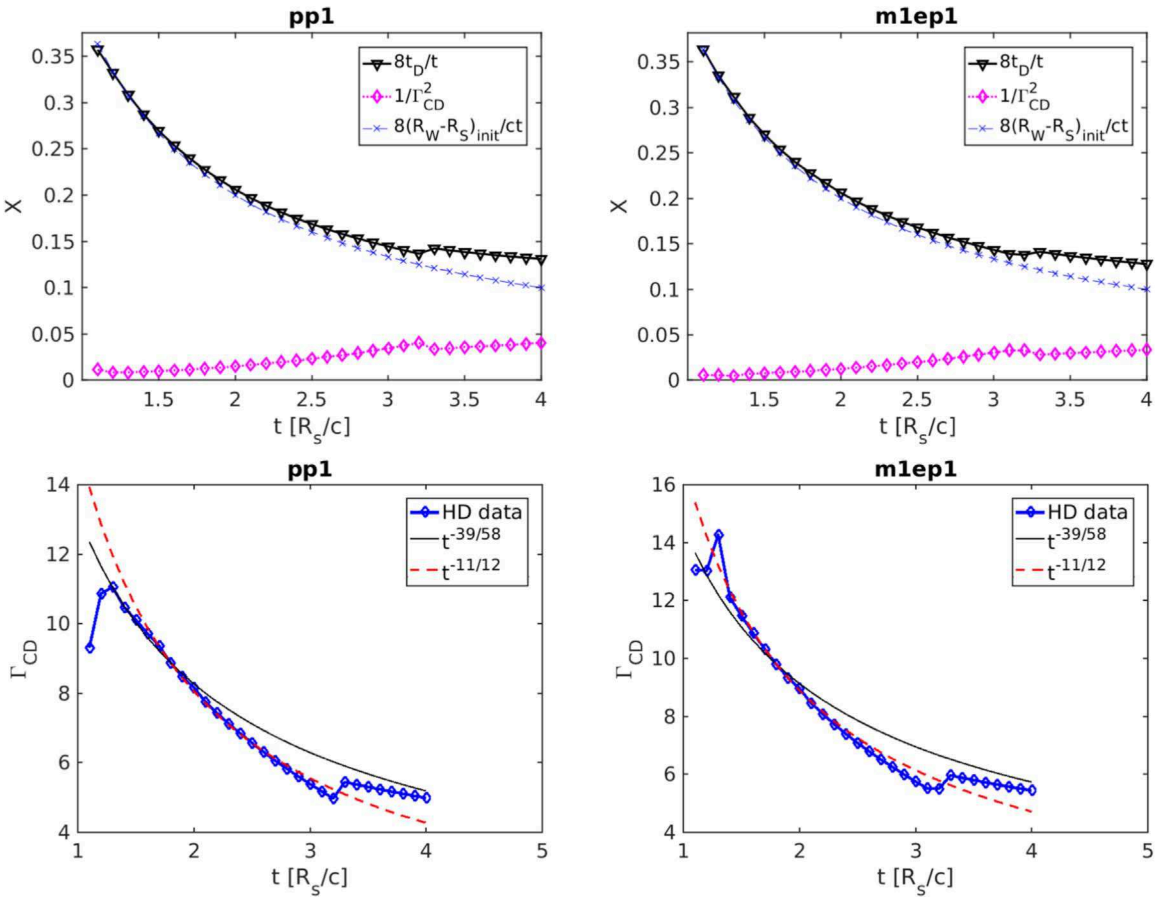

Figure 10. Effects of magnetization on flow dynamics. Top row: self-similar coordinate of the second shock χ (same as in Figure 3) for cases with magnetization $\sigma_{\rm w} = 0$ (left) and $\sigma_{\rm w} = 10$ (right). Bottom row: Lorentz factor as a function of time—triangles and analytical expectations (Lyutikov 2017) for cases with magnetization $\sigma_{\rm w} = 0$ (left) and $\sigma_{\rm w} = 10$ (right). The jumps in the Lorentz factor at later times occur when the wind-driven FS catches up with the leading BMFS.

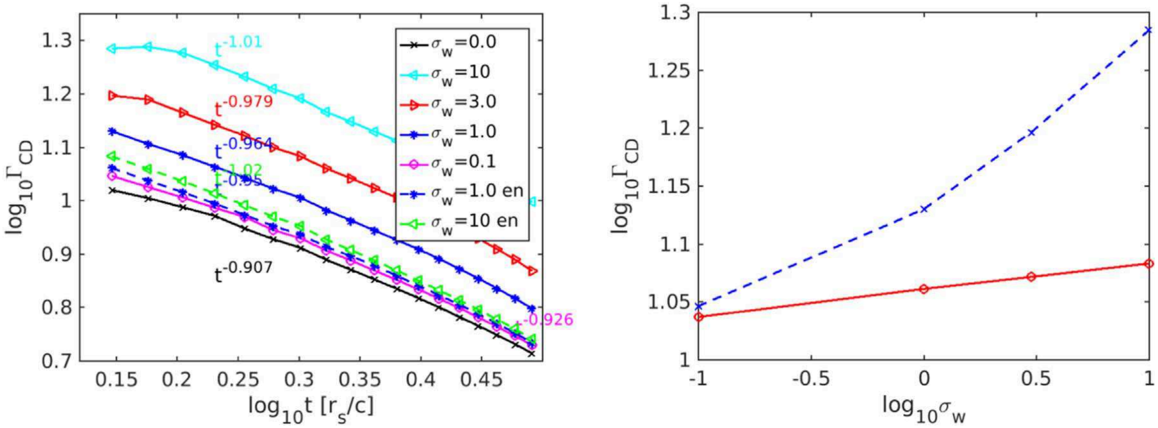

Figure 11. The Lorentz factor of the CD as function of time, left panel, (see Equation (12) $\Gamma_{\rm CD} \propto t^{-0.92}$). We calculate the power indexes on the straight parts of the curves, $0.25 < \log_{10} t < 0.45$. Dependence of the Lorentz factor of the CD on wind magnetization at $t = 1.4[R_s/c]$, right panel. The red curve represents the constant total power, the blue dashed curve represents the constant matter power. As expected, for the fixed total power the Lorentz factor of the CD is approximately independent of the the wind magnetization.

time-of-flight effects (e.g., Fenimore et al. 1996; Nakar et al. 2003; Piran 2004).

The intrinsic emissivity at time t' depends on the distribution function N and synchrotron power P_ω:

$$L'(\omega', t') = \int\int N_A(\gamma', t') P_\omega(\omega')\, d\gamma' dA', \tag{24}$$

where N_A, the number of particles per unit area, is defined as $N_A = N/A = N/(2\pi r'^2(1 - \cos\theta_j))$, $P(\omega')$ is the power per unit frequency emitted by each electron, and dA' is the surface differential (unlike Fenimore et al. 1996, we do not have extra $\cos\theta$ in the expression for the area since we use volumetric emissivity, not emissivity from a surface).

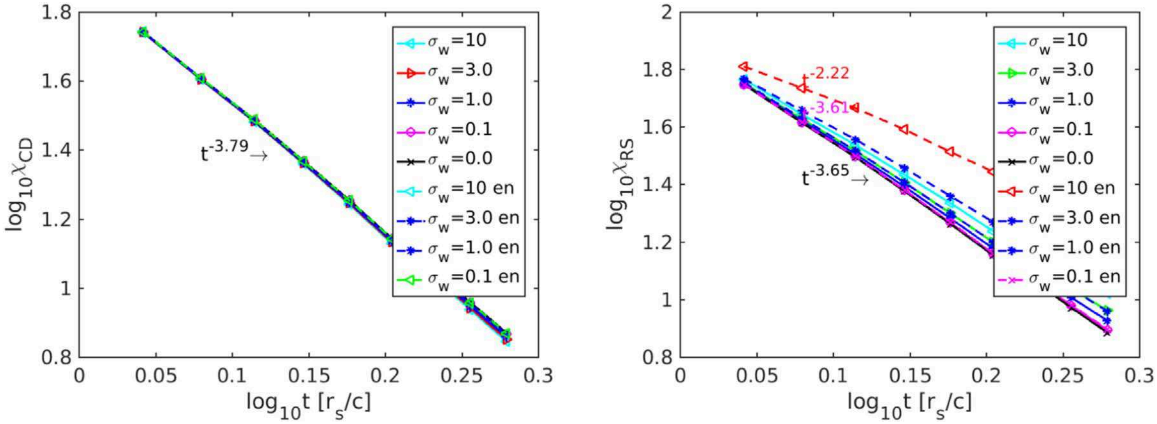

Figure 12. Time dependence of $\chi_{\rm CD}$ (see Equation (11)) and $\chi_{\rm RS}$ (location of the CD and RS in a self-similar coordinate). In a fully self-similar regime, the dynamics of the RS follows that of the CD. The low σ models do show this property. As we discussed above, in the case of the CD, for smaller wind powers the effective time delay t_d starts to become important, resulting in smaller temporal indexes. We attribute the flatter dependence of $\chi_{\rm CD}$ on time (see also Figure 13) to a somewhat similar effect: for larger σ, the RS Lorentz factor is smaller, $\propto \Gamma_{\rm CD}/\sqrt{\sigma}$. Thus, beyond some value of σ the Lorentz factor of the RS and the corresponding $\chi_{\rm CD}$ demonstrate flatter temporal profiles.

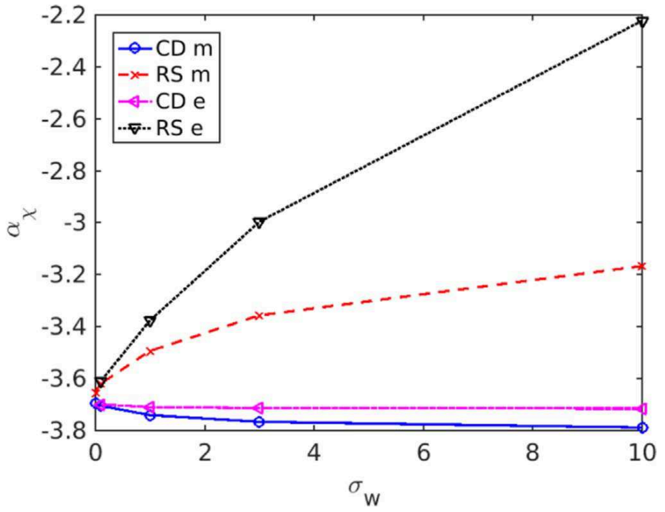

Figure 13. Dependence of α_χ on the magnetization of the wind ($\chi_{\rm CD} \propto t^{\alpha_\chi}$). Diamonds and crosses correspond to the CD and RS in the case of a preserved energy flux of hydrodynamical flux in the wind. The right triangle and the inverted triangle correspond to the case of preserved total energy flux in the wind (see caption for Figure 12).

We assume that the observer is located on the symmetry axis and that the active part of the RS occupies angle θ_j to the line of sight. The emitted power is then

$$L'(\omega', t') = \int_0^{\theta_j} \int_{\gamma'_{\min}}^{\infty} N_A(\gamma', t') P(\omega') d\gamma' 2\pi r'^2 \sin(\theta) d\theta. \tag{25}$$

Photons seen by a distant observer at times $T_{\rm ob}$ are emitted at different radii and angles θ. To take into account the time-of-flight effects, we note that the distance between the initial explosion point and an emission point (r', θ) is $r' = vt' = vT_{\rm ob}(1 - \beta\cos(\theta))^{-1}\gamma_{\rm RS}^{-1}$, where $T_{\rm ob}$ is the observed time. Suppose that a photon was emitted from the distance r' and angle $\theta = 0$ at time t', and at the same time, the other photon was emitted from the distance r' and any arbitrary angle $\theta = \theta_i < \theta_j$. These two photons will be observed at time T_0 and T_{θ_i}, and then the relation between T_0 and T_{θ_i} is given by

$$r' = vt' = \frac{vT_0}{(1 - \beta)\gamma_{\rm RS}} = \frac{vT_{\theta_i}}{(1 - \beta\cos(\theta_i))\gamma_{\rm RS}}, \tag{26}$$

where the time t' measured in the fluid frame, and the corresponding observed time $T_{\rm ob}$, is a function of θ and t':

$$T_{\rm ob} = t(1 - \beta\cos\theta) = t'(1 - \beta\cos\theta)\gamma_{\rm RS}. \tag{27}$$

Taking the derivative of Equation (27), we find

$$\sin(\theta)d\theta = -\frac{T_{\rm ob}}{t'^2\beta\gamma_{\rm RS}}dt' \approx -\frac{T_{\rm ob}}{t'^2\gamma_{\rm RS}}dt'. \tag{28}$$

Substituting relation (28) into (25), the observed luminosity becomes

$$L'(T_{\rm ob}, \omega') \approx \int_{t'_{\theta'=0}}^{t'_{\theta'=\theta_j}} \int_{\gamma'_{\min}}^{\infty} \frac{2\pi c^2 T_{\rm ob}}{\gamma_{\rm RS}} \times N_A(\gamma', t') P(\omega') d\gamma' dt'. \tag{29}$$

To understand Equation (29), the radiation observed at $T_{\rm ob}$ corresponds to the emission angle from 0 to θ_j, which also corresponds to the emission time $t'_{\theta'=0} = T_{\rm ob}/(1 - \beta)\gamma_{\rm RS}$ to $t'_{\theta'=\theta_j} = T_{\rm ob}/(1 - \beta\cos\theta_j)\gamma_{\rm RS}$. So we need to integrate the emissivity function over the range of the emission angle, or integrate the emissivity function over the range of the emission time from $t'_{\theta'=0} = T_{\rm ob}/(1 - \beta)\gamma_{\rm RS}$ to $t'_{\theta'=\theta_j} = T_{\rm ob}/(1 - \beta\cos\theta_j)\gamma_{\rm RS}$.

Finally, taking into account Doppler effects (Doppler shift $\omega = \delta\omega'$ and the intensity boost $I_\omega(\omega) = \delta^3 I'_{\omega'}(\omega')$, where δ is the Doppler factor $\delta = 1/(\gamma_{\rm RS}(1 - \beta\cos\theta))$), substituting the relation $t' = T_{\rm ob}/(1 - \beta\cos(\theta))\gamma_{\rm RS}$ into Equation (29), we finally arrive at the equation for the observed spectral luminosity:

$$F_\omega = \int_{\frac{T_{\rm ob}}{(1-\beta\cos(\theta_j))\gamma_{\rm RS}}}^{\frac{T_{\rm ob}}{(1-\beta)\gamma_{\rm RS}}} \times \int_{\gamma'_{\min}}^{\infty} \frac{1}{2\gamma_{\rm RS}} c^2 D^{-2} T_{\rm ob} \delta^3 N_A P(\omega/\delta) d\gamma' dt', \tag{30}$$

where D is the distance to the GRB.

Next we apply these general relations to three specific problem: (i) origin of plateaus in afterglow light curves;

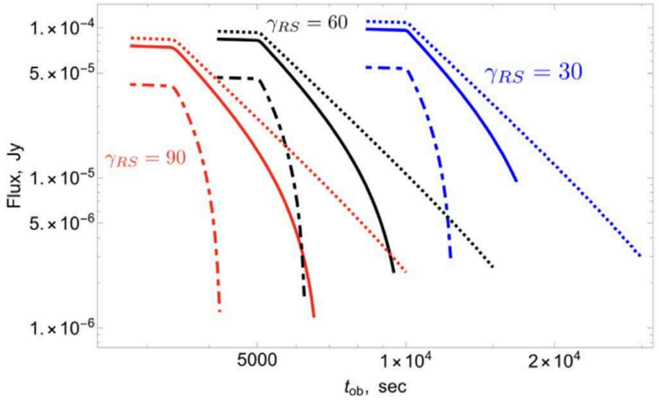

Figure 14. The light curve at 100 keV for different Lorentz factors of the post-RS flow and different jet angles $2/\gamma_{\rm RS}$ (dotted curve), $1/\gamma_{\rm RS}$ (solid curve), $1/(2\gamma_{\rm RS})$ (dotted–dashed curve), and different Lorentz factors of the RS. For $\theta_j \leqslant 1/\gamma_{\rm RS}$, the drop in intensity is extremely fast.

(ii) sudden drops in the afterglow light curves, Section 5.3; and (iii) afterglow flares, Section 5.4. For numerical estimates, we assume the redshift $z = 1$, the Lorentz factor of the wind $\gamma_w = 5 \times 10^5$, the wind luminosity $L_w = 10^{46}$ erg s^{-1}, the initial injection time $t_0' = 10^5$ s (in jet frame), and the power-law index of particle distribution $p = 2.2$, and the viewing angle is 0 (observer on the axis) for all calculations.

5.3. Results: Plateaus and Sudden Intensity Drops in Afterglow Light Curves

Particles accelerated at the RS emit in the fast-cooling regime. The resulting synchrotron luminosity L_s is approximately proportional to the wind luminosity, L_w, as discussed by Lyutikov & Camilo Jaramillo (2017). (For highly magnetized winds with $\sigma \gg 1$, the RS emissivity is only mildly suppressed, by high magnetization, $\propto 1/\sqrt{\sigma}$, due to the fact that higher sigma shocks propagate faster with respect to the wind.) Thus, the constant wind will produce a nearly constant light curve: plateaus are natural consequences in our model in the case of constant long-lasting wind, see Figure 14. At early times, all light curves show a nearly constant evolution with time and a plateau, with a flux of $\propto t_{\rm ob}^{-0.1}$. A slight temporal decrease is due to the fact that magnetic field at the RS decreases with time so that particles emit less efficiently. This observed temporal decrease is flatter than what is typically observed, $\propto t_{\rm ob}^{-\alpha_2}$ with $\alpha_2 = 0.5$–1 (Nousek et al. 2006). A steeper decrease can be easily accommodated due to the decreasing wind power. This explains the plateaus.

Next we assume that the central engine suddenly stops operating. This process could be due to the collapse of a neutron star into a black hole or sudden depletion of an accretion disk. At a later time, when the "tail" of the wind reaches the termination shock, acceleration stops. Let the injection terminate at a some time $t_{\rm stop}'$. The distribution function in the shocked part of the wind then becomes

$$N(\gamma', t') \propto \int_{t_0'}^{\min(t', t_{\rm stop}')} G(\gamma', t', t_i')dt_i'. \tag{31}$$

Figure 15 shows the evolution of the distribution function by assuming the Lorentz factor of the RS of $\gamma_{\rm RS} = 90$, and the injection is stopped at time $t_{\rm stop}' = 1.5 \times 10^5$ s (in this case, the $T_{\rm ob,stop} = 833$ s is in the observer's frame). The number of high energy particles drops sharply right after the injection is stopped: particles lose their energy via synchrotron radiation and adiabatic expansion in the fast-cooling regime.

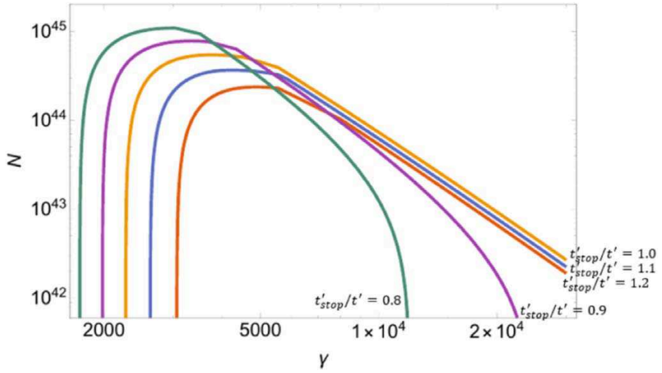

Figure 15. Evolution of the distribution function. Here we take account the effect of radiation loss and adiabatic expansion. In our calculation, the Lorentz factor of the RS is $\gamma_{\rm RS} = 90$ and the injection is stopped at time $t_{\rm stop}' = 1.5 \times 10^5$ s, $\gamma_{\rm min} = \gamma_w/\gamma_{\rm RS} = 5.5 \times 10^3$, initial magnetic field $B_0 = 2.1$ G. The times are measured in a fluid frame at $t_{\rm stop}'/t' = 1.2$, 1.1, 1.0, 0.9, 0.8 from the red to the green curves.

The resulting light curves are plotted in Figure 14. We assume a post-RS flow of $\gamma_{\rm RS} = 30$, 60, 90 and three jet opening angles of $\sim(1/2, 1, 2) \times \gamma_{\rm RS}^{-1}$. These particular choices of θ_j are motivated by our expectation that sudden switch-off of the acceleration at the RS will lead to fast decays in the observed flux (in the fast-cooling regime).

The injection is stopped at a fixed time in the fluid frame, corresponding to $t_0' = 6 \times 10^5$ s. There is a sudden drop in the intensity when the injection is stopped ($T_{\rm ob} = 10,000$ s, blue curve; $T_{\rm ob} = 5000$ s, black curve; and $T_{\rm ob} = 3 \times 10^3$ s, red curve). The blue curve represents $\gamma_{\rm RS} = 30$, $\gamma_{\rm min} = \gamma_{\rm w}/\gamma_{\rm RS} = 1.65. \times 10^4$ and an initial magnetic field of $B_0 =$ 6.4 G; the green curve represents $\gamma_{\rm RS} = 60$, $\gamma_{\rm min} = \gamma_w/\gamma_{\rm RS} = 8.3 \times 10^3$and an initial magnetic field of $B_0 = 3.2$ G; and the red curve represents $\gamma_{\rm RS} = 90$, $\gamma_{\rm min} = \gamma_w/\gamma_{\rm RS} = 5.5 \times 10^3$ and an initial magnetic field of $B_0 = 2.1$ G. Here we assume $B_0 \propto \gamma_{\rm RS}^{-1}$ for our calculations. A smaller jet angle produces a sharper drop.

In the simplest qualitative explanation, consider a shell of radius $r_{\rm em}$ extending to a finite angle θ_j and producing an instantaneous flash of emission (instantaneous is an approximation of the fast-cooling regime). The observed light curve is then (Fenimore et al. 1996)

$$\propto \begin{cases} \left(\frac{T_{\rm ob}}{T_0}\right)^{-(\alpha+2)}, & 0 < T_{\rm ob} < \frac{r_{\rm em}/c}{2}\theta_j^2 \\ 0 & \frac{r_{\rm em}/c}{2}\theta_j^2 < T_{\rm ob} \end{cases}, \tag{32}$$

where $T_0 = \frac{r_{\rm em}/c}{2\gamma_{\rm RS}^2}$ and α is the spectral index. Thus, for $\theta_j > 1/\gamma_{\rm RS}$ the observed duration of a pulse is $\sim T_0$, while for $\theta_j < 1/\gamma_{\rm RS}$ the duration of the pulse is much shorter, $\sim T_0(\theta_j\gamma_{\rm RS})^2 \ll T_0$. Thus, in this case a drop in intensity is faster than what would be expected in either faster shocks or shocks producing emission in the slow-cooling regime.

5.4. Results: Afterglow Flares

Next, we investigate the possibility that afterglow flares are produced due to the variations in wind power. We reconsider

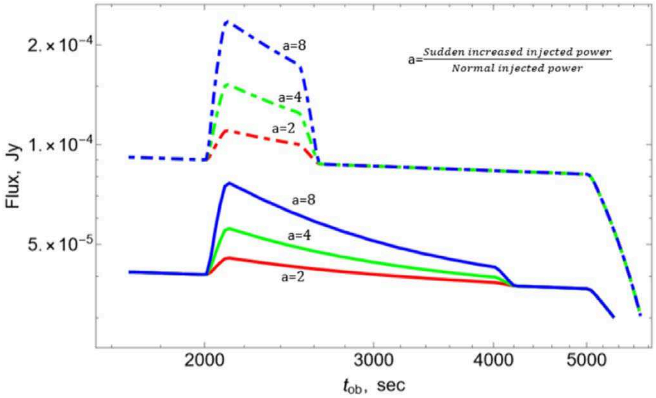

Figure 16. Afterglow flares due to variations in wind luminosity for the case of $\gamma_{\mathrm{RS}} = 60$ (green curve in the Figure 14). The ejected power is increased by factors of $a = 2, 4, 8$ for a short period from 2.4×10^5–2.5×10^5 s (in the fluid frame). The solid lines represent $\theta_j = \gamma_{\mathrm{RS}}$, and the dashed lines represent $\theta_j = 1/2\gamma_{\mathrm{RS}}$. For clarity, the relative shift of intensities between the plots for two opening angles is due to our parameterization of the injected power (constant total power not isotropic equivalent).

the case of $\gamma_{\mathrm{RS}} = 60$ (the green curve in Figure 14), but set the ejected power at 2, 4, and 8 times larger than the average power for a short period of time from 2.4×10^5–2.5×10^5 s. We consider the two cases: the wide jet angle ($\theta_j = 1/\gamma_{\mathrm{RS}}$) and the narrow jet angle ($\theta_j = 1/2\gamma_{\mathrm{RS}}$). The corresponding light curves are plotted in Figure 16.

Light curves show a sharp rise around $T_{\mathrm{ob}} = 2000$, corresponding to the increased ejected power of $t = 2.4 \times 10^5$ s at emission angle $\theta = 0$, followed by a sharp drop around $T_{\mathrm{ob}} = 4000$ s for the case of the wide jet and $T_{\mathrm{ob}} = 2500$ s for the case of the narrow jet (which corresponds to the ending time of the increased ejected power of $t = 2.5 \times 10^5$ s at the emission angle $\theta = \theta_j$). Bright flares can clearly be seen. Importantly, the corresponding total injected energy is only $\sim$1%, 5%, and 10% larger than the average value. The magnitude of the rise in flux is less than the magnitude of the rise in ejected power (e.g., the rise in ejected power by a factor 8 only produces the rise in flux by a factor 2), due to the fact that the emission from the increased ejected power from different angles is spread out in observer time. Thus, variations in the wind power, with minor total energy input, can produce bright afterglow flares (Lyutikov 2006b).

6. Discussion

In this paper we have discussed the properties of GRB afterglows within the pulsar-wind paradigm: long-lasting, ultrarelativistic, highly magnetized wind with particles accelerated at the wind termination shock (Kennel & Coroniti 1984a). The present model of long-lasting winds in GRBs is qualitatively different from previous models based on the fireball paradigm, see Section 2.

We first performed a set of detailed relativistic magnetohydrodynamics simulations of relativistic double explosions. Our numerical results are in excellent agreement with theoretical prediction (Lyutikov 2017; Lyutikov & Camilo Jaramillo 2017). For example, for sufficiently high wind power we have $\Gamma_{\mathrm{CD}} \propto t^{-11/12}$, while after t_{eq} the shocks merge and move as a single self-similar shock with $\Gamma_{\mathrm{CD}} \propto t^{-1/2}$. In addition, the numerics demonstrate a much richer set of phenomena (e.g., transitions between various analytical limits and variations in the temporal slopes). We find that even for the case of constant external density and constant wind power the dynamics of the wind termination shock shows a large variety—both in temporal slopes of the scaling of the Lorentz factor of the shock and in producing non-monotonic behavior. Non-self-similar evolution of the wind termination shock occurs for two different reasons: (i) at early times due to a delay in the activation of the long-lasting fast wind; (ii) at late times when the energy injected by the wind becomes comparable to the energy of the initial explosion.

Second, we performed radiative calculations of the RS emission and demonstrated that emission from the long-lasting relativistic wind can resolve a number of contradicting GRB observations. We can reproduce:

1. Afterglow plateaus: In the fast-cooling regime the emitted power is comparable to the wind power. Hence, only mild wind luminosity $L_w \sim 10^{46}$ erg s^{-1} is required (isotropic equivalent).
2. Sudden drops in afterglow light curves: If the central engine stops operating, and if at the corresponding moment the Lorentz factor of the RS is of the order of the jet angle, a sudden drop in intensity will be observed.
3. Afterglow flares: If the wind intensity varies, this leads to the sharp variations of afterglow luminosities. Importantly, the total injected *energy* is small compared to the total energy of the explosion.

Lyutikov & Camilo Jaramillo (2017) also discussed how the model provides explanations for a number of other GRB phenomena, like the problem of "naked GRBs" (Page et al. 2006; Vetere et al. 2008) (if the explosion does not produce a long-lasting wind, then there will be no X-ray afterglow since the RS reflects the properties of wind), "missing orphan afterglows": both prompt emission and afterglow emission arise from the engine-powered flow, so they may have similar collimation properties. The model also offers explanations for missing and/or chromatic jet breaks, orphan afterglows, "missing" reverse shocks (they are not missing—they are dominant).

In conclusion, the high energy emission from highly relativistic wind is (i) highly efficient; (ii) can be smooth (over a period of time) for constant wind parameters; and (iii) can react quickly to the changes in the wind properties. The RS also contributes to the optical—this explains the correlated X-optical features often seen in afterglows. FS emission occurs in the optical range, and at later times, in radio (Lyutikov & Camilo Jaramillo 2017).

We thank the PLUTO team for the use of the PLUTO code and for technical support. The visualization of the results was performed in the VisIt package (Hank Childs et al. 2012). This work had been supported by NASA grants 80NSSC17K0757 and 80NSSC20K0910, NSF grants 10001562 and 10001521, and NASA Swift grant 1619001

The data that support the findings of this study are available from the corresponding author upon reasonable request.

Appendix
Simulation Profiles

A.1. Unmagnetized Cases

As can be seen in Figure 17, from the *pm*2 to the *pp*2 model, with increasing wind power, the Lorentz factor of the FS and

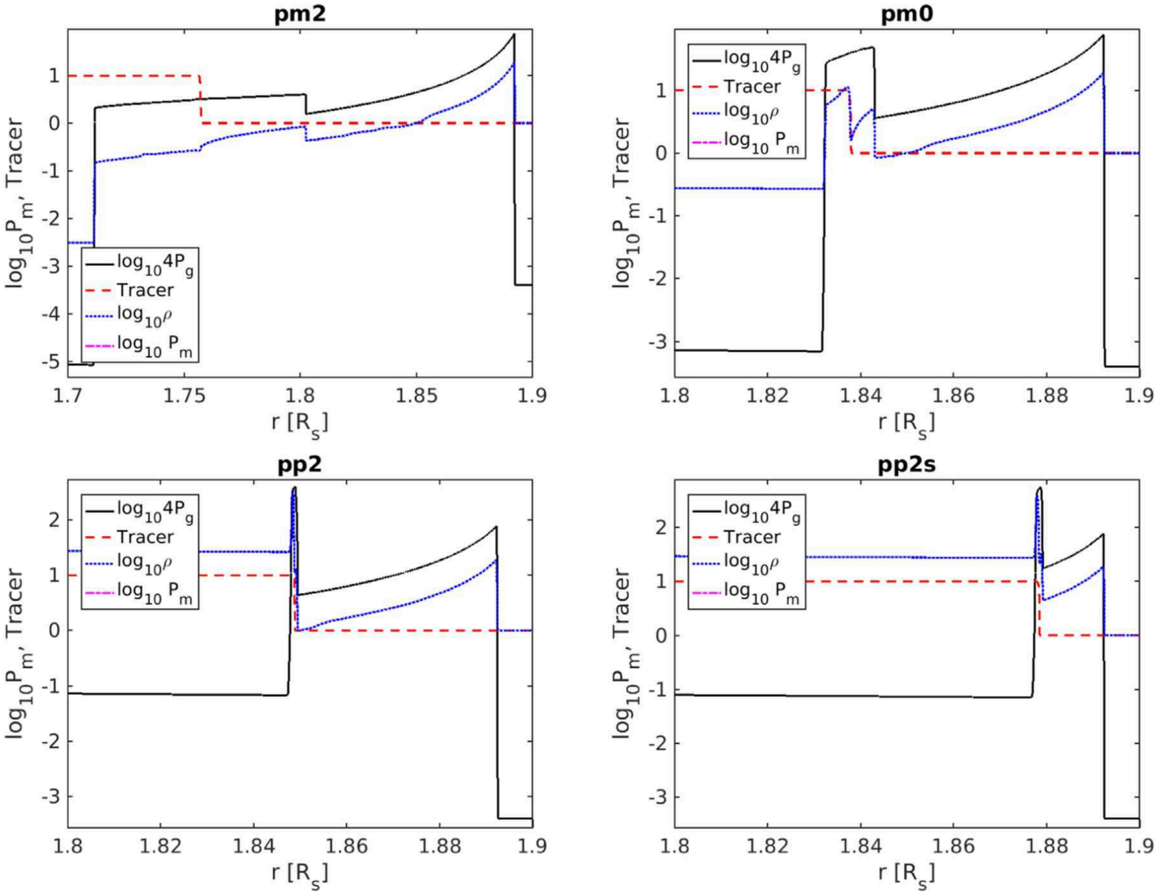

Figure 17. Gas pressure (thick solid lines), density (dotted line), and tracer (dashed line) as functions of radius at the moment $t = 1.9$ $[r_s/c]$.

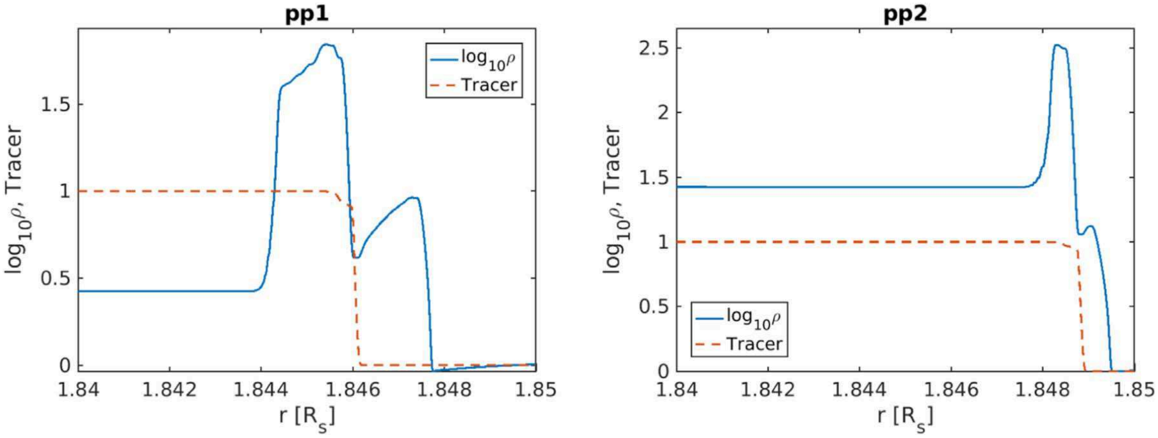

Figure 18. Zoom-in to the region close to the CD: density (solid line) and tracer (dashed line) as functions of radius at the moment $t = 1.9$ $[r_s/c]$.

the RS also increase, while the distance between these shocks becomes smaller, where positions of the shocks are indicated by jumps in pressure; the jump in density at constant pressure identifies the CD. The shift of the wind injection radius (compare models *pm*2 and *pm*2*s* or *pp*2 and *pp*2*s*) do not change the structure of the solution significantly. The change in the injection radius shift the position of the shocked wind structure as a whole. High resolution of our setup allows to resolve structures of density distribution on the radial scale $\sim 10^{-4}$ r_s (see Figure 18).

A.2. Magnetized Cases

Figures 19–21 demonstrate the weak dependence of the density profile of the double shocked matter if the total energy of the wind is preserved. On the other hand, when we preserved the hydrodynamic energy flux in the wind and increased its magnetization, due to increasing of the total power, the wind-double-shocked matter suffered from stronger compression and the double-shocked-layered matter became thinner. On the other hand, an increase in magnetization decreases the compression ratio of the shocked wind.

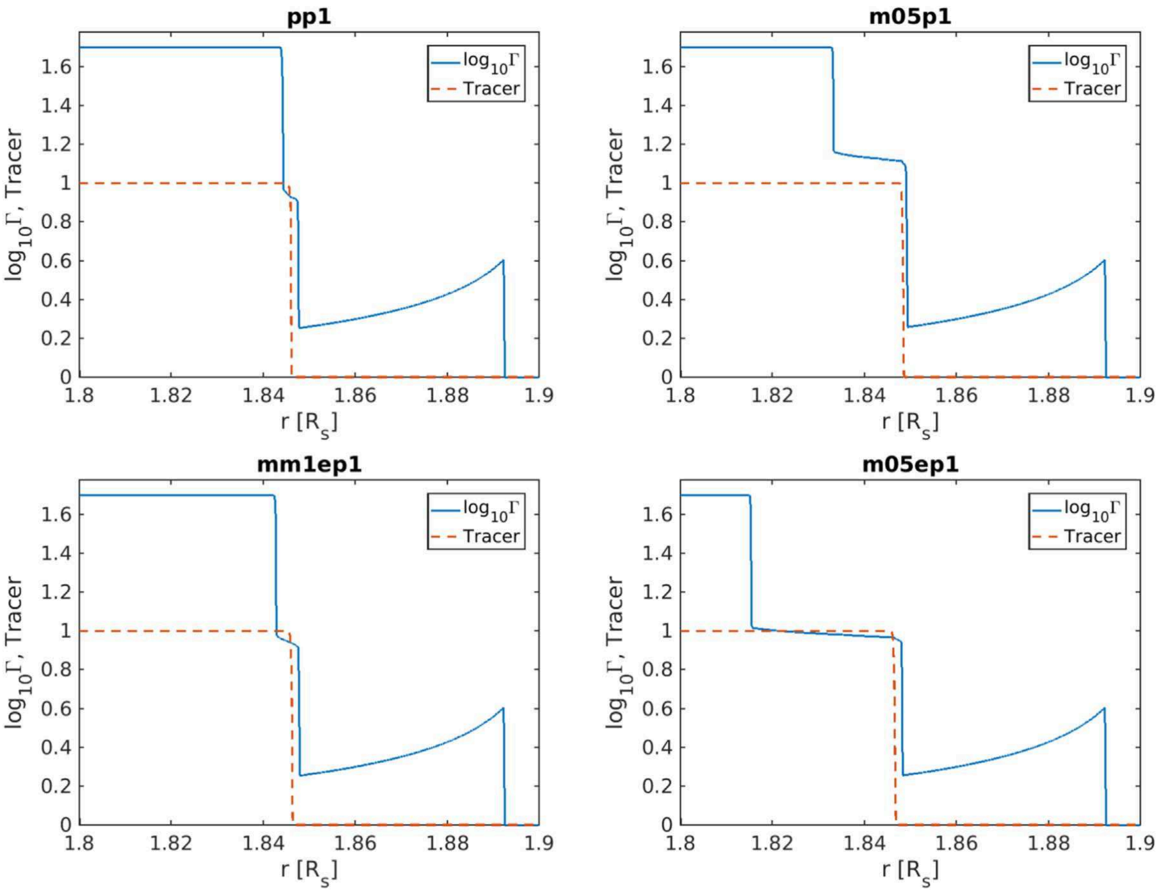
pp1

m05p1

mm1ep1

m05ep1

Figure 19. Lorentz factor and tracer distribution as functions of radius at the moment $t = 1.9$ for models with different magnetizations.

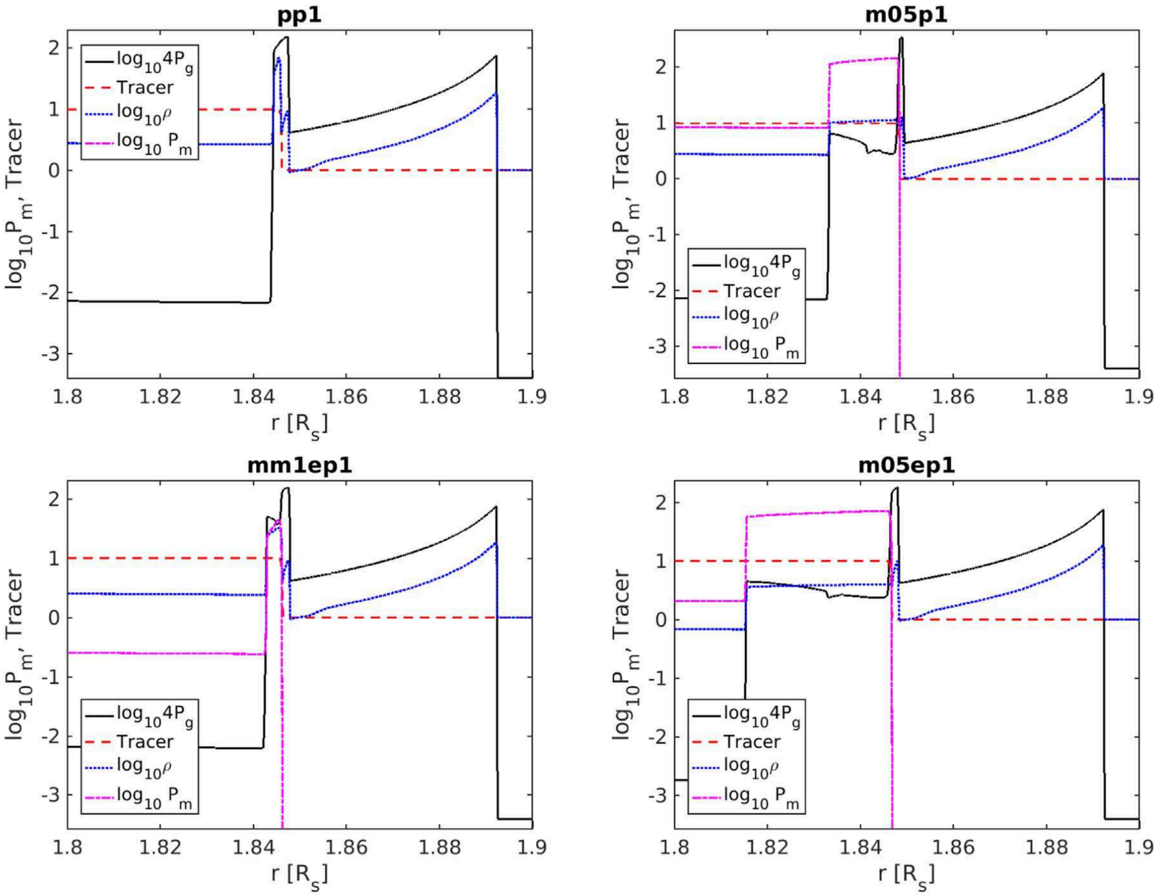

Figure 20. Gas pressure (thick solid line), density (dotted line), and tracer (dashed line) as functions of radius at the moment $t = 1.9$ for models with different magnetizations.

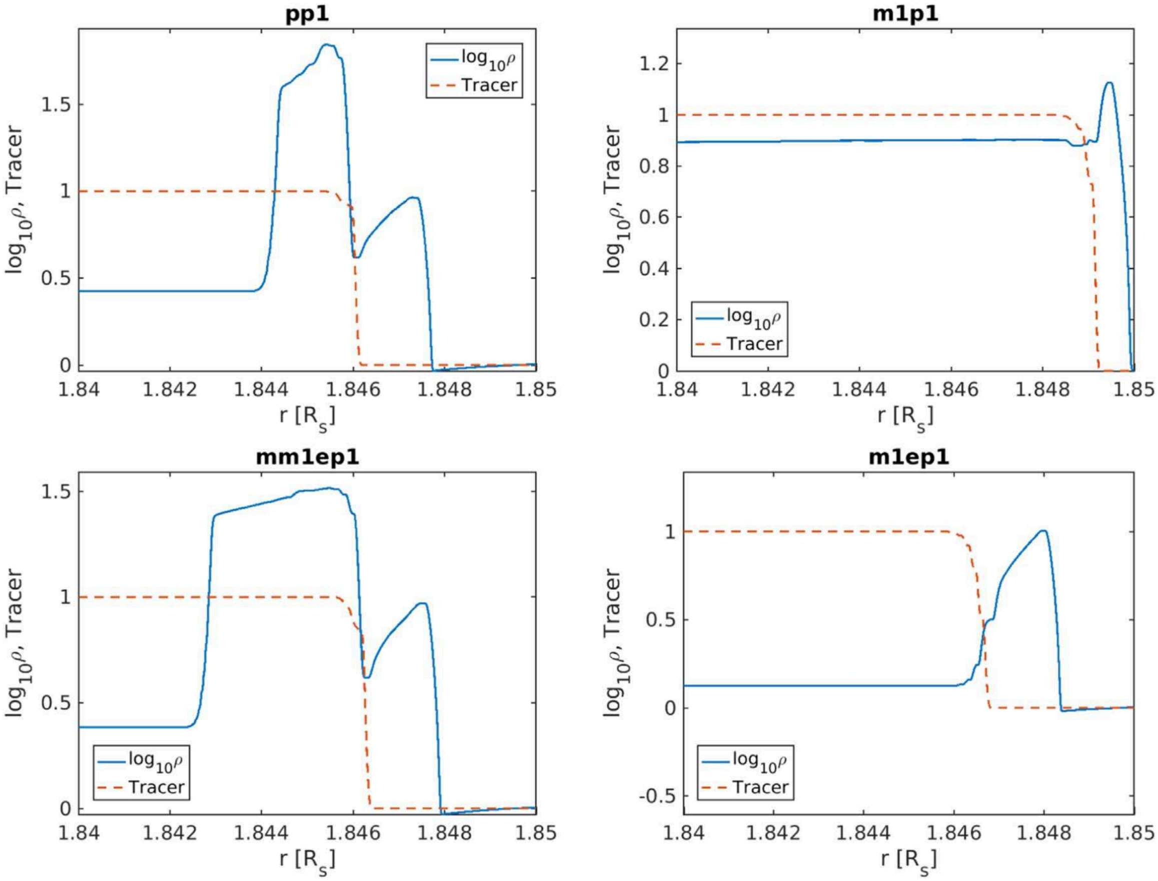

Figure 21. Zoom-in to the regions near the CD. Density (solid line) and tracer (dashed line) as functions of radius at the moment $t = 1.9$ for cases with different magnetizations.

ORCID iDs

Maxim V. Barkov https://orcid.org/0000-0002-0960-5407
Maxim Lyutikov https://orcid.org/0000-0001-6436-8304

References

Barkov, M. V., & Komissarov, S. S. 2010, MNRAS, 401, 1644
Barkov, M. V., & Pozanenko, A. S. 2011, MNRAS, 417, 2161
Beniamini, P., & Mochkovitch, R. 2017, A&A, 605, A60
Blandford, R. D., & McKee, C. F. 1976, PhFl, 19, 1130
Cannizzo, J. K., & Gehrels, N. 2009, ApJ, 700, 1047
Chincarini, G., Mao, J., Margutti, R., et al. 2010, MNRAS, 406, 2113
Dai, Z. G. 2004, ApJ, 606, 1000
Dai, Z. G., & Lu, T. 1998, A&A, 333, L87
de Pasquale, M., Evans, P., Oates, S., et al. 2009, MNRAS, 392, 153
de Pasquale, M., Oates, S. R., Page, M. J., et al. 2007, MNRAS, 377, 1638
de Pasquale, M., Page, M. J., Kann, D. A., et al. 2016, MNRAS, 462, 1111
Fenimore, E. E., Madras, C. D., & Nayakshin, S. 1996, ApJ, 473, 998
Gat, I., van Eerten, H., & MacFadyen, A. 2013, ApJ, 773, 2
Gehrels, N., & Razzaque, S. 2013, FrPhy, 8, 661
Genet, F., Daigne, F., & Mochkovitch, R. 2007, MNRAS, 381, 732
Gomboc, A., Kobayashi, S., Mundell, C. G., et al. 2009, in AIP Conf. Ser., 1133, ed. C. Meegan, C. Kouveliotou, & N. Gehrels (Melville, NY: AIP), 145
Hank Childs, H., Brugger, E., Whitlock, B., et al. 2012, High Performance Visualization-Enabling Extreme-Scale Scientific Insight (Boca Raton, FL: CRC Press), 357
Hascoët, R., Beloborodov, A. M., Daigne, F., & Mochkovitch, R. 2017, MNRAS, 472, L94
Ito, H., Matsumoto, J., Nagataki, S., et al. 2019, NatCo, 10, 1504
Johnson, M. H., & McKee, C. F. 1971, PhRvD, 3, 858
Kann, D. A., Klose, S., Zhang, B., et al. 2010, ApJ, 720, 1513
Kardashev, N. S. 1962, SvA, 6, 317
Kargaltsev, O., & Pavlov, G. G. 2008, in AIP Conf. Ser., 983, 40 Years of Pulsars: Millisecond Pulsars, Magnetars and More, ed. C. Bassa et al. (Melville, NY: AIP), 171
Kennel, C. F., & Coroniti, F. V. 1984a, ApJ, 283, 710
Kennel, C. F., & Coroniti, F. V. 1984b, ApJ, 283, 694
Khangulyan, D., Aharonian, F., Romoli, C., & Taylor, A. 2020, arXiv:2003.00927
Khangulyan, D., Koldoba, A. V., Ustyugova, G. V., Bogovalov, S. V., & Aharonian, F. 2018, ApJ, 860, 59
Komissarov, S. S., & Barkov, M. V. 2007, MNRAS, 382, 1029
Komissarov, S. S., & Barkov, M. V. 2009, MNRAS, 397, 1153
Krimm, H. A., Boyd, P., Mangano, V., et al. 2007a, GCN, 6014, 1
Krimm, H. A., Boyd, P., Mangano, V., et al. 2007b, GCNR, 26, 2
Lang, K. R. 1999, Astrophysical Formulae (New York: Springer)
Lien, A., Sakamoto, T., Barthelmy, S. D., et al. 2016, ApJ, 829, 7
Lyons, N., O'Brien, P. T., Zhang, B., et al. 2010, MNRAS, 402, 705
Lyutikov, M. 2006a, NJPh, 8, 119
Lyutikov, M. 2006b, MNRAS, 369, L5
Lyutikov, M. 2009, arXiv:0911.0349
Lyutikov, M. 2010, PhRvE, 82, 056305
Lyutikov, M. 2011, PhRvD, 83, 124035
Lyutikov, M. 2017, PhFl, 29, 047101
Lyutikov, M., & Blandford, R. 2003, arXiv:astro-ph/0312347
Lyutikov, M., & Camilo Jaramillo, J. 2017, ApJ, 835, 206
Lyutikov, M., & McKinney, J. C. 2011, PhRvD, 84, 084019
Mazaeva, E., Pozanenko, A., & Minaev, P. 2018, IJMPD, 27, 1844012
Mészáros, P. 2006, RPPh, 69, 2259
Mignone, A., Bodo, G., Massaglia, S., et al. 2007, ApJS, 170, 228
Mignone, A., Ugliano, M., & Bodo, G. 2009, MNRAS, 393, 1141
Mimica, P., Giannios, D., & Aloy, M. A. 2009, A&A, 494, 879
Nakar, E., Piran, T., & Granot, J. 2003, NewA, 8, 495
Nousek, J. A., Kouveliotou, C., Grupe, D., et al. 2006, ApJ, 642, 389
Oates, S. R., de Pasquale, M., Page, M. J., et al. 2007, MNRAS, 380, 270
O'Brien, P. T., Willingale, R., Osborne, J., et al. 2006, ApJ, 647, 1213
Oganesyan, G., Ascenzi, S., Branchesi, M., et al. 2020, ApJ, 893, 88
Paczynski, B. 1986, ApJL, 308, L43

Page, K. L., King, A. R., Levan, A. J., et al. 2006, ApJL, 637, L13
Panaitescu, A. 2007, MNRAS, 380, 374
Panaitescu, A., Mészáros, P., Gehrels, N., Burrows, D., & Nousek, J. 2006, MNRAS, 366, 1357
Panaitescu, A., Mészáros, P., & Rees, M. J. 1998, ApJ, 503, 314
Piran, T. 1999, PhR, 314, 575
Piran, T. 2004, RvMP, 76, 1143
Porth, O., Komissarov, S. S., & Keppens, R. 2014, MNRAS, 438, 278
Racusin, J. L., Liang, E. W., Burrows, D. N., et al. 2009, ApJ, 698, 43
Rees, M. J., & Meszaros, P. 1992, MNRAS, 258, 41P
Rees, M. J., & Meszaros, P. 1994, ApJL, 430, L93
Rees, M. J., & Mészáros, P. 1998, ApJL, 496, L1
Resmi, L., & Zhang, B. 2016, ApJ, 825, 48
Rowlinson, A., O'Brien, P. T., Metzger, B. D., Tanvir, N. R., & Levan, A. J. 2013, MNRAS, 430, 1061
Rowlinson, A., O'Brien, P. T., Tanvir, N. R., et al. 2010, MNRAS, 409, 531
Sari, R., & Piran, T. 1995, ApJL, 455, L143
Sari, R., & Piran, T. 1999, ApJL, 517, L109
Sari, R., Piran, T., & Narayan, R. 1998, ApJL, 497, L17
Sbarufatti, B., Mangano, V., Mineo, T., Cusumano, G., & Krimm, H. 2007, GCN, 6008, 1
Sironi, L., & Spitkovsky, A. 2011, ApJ, 741, 39
Troja, E., Cusumano, G., O'Brien, P. T., et al. 2007, ApJ, 665, 599
Uhm, Z. L., & Beloborodov, A. M. 2007, ApJL, 665, L93
Uhm, Z. L., Zhang, B., Hascoët, R., et al. 2012, ApJ, 761, 147
Usov, V. V. 1992, Natur, 357, 472
van Eerten, H. 2014, MNRAS, 442, 3495
Vetere, L., Burrows, D. N., Gehrels, N., et al. 2008, in Gamme Ray Bursts, AIP Conf. Proc. 1000, ed. M. Galassi, D. Palmer, & E. Fenimore (Melville, NY: AIP), 191
Warren, D. C., Barkov, M. V., Ito, H., Nagataki, S., & Laskar, T. 2018, MNRAS, 480, 4060
Warren, D. C., Beauchemin, C. A. A., Barkov, M. V., & Nagataki, S. 2021, ApJ, 906, 33
Warren, D. C., Ellison, D. C., Barkov, M. V., & Nagataki, S. 2017, ApJ, 835, 248